SMART COMPOSITES WITH TUNABLE STRESS-STRAIN CURVES

A THESIS SUBMITTED TO
THE GRADUATE SCHOOL OF ENGINEERING AND SCIENCE
OF BILKENT UNIVERSITY
IN PARTIAL FULFILLMENT OF THE REQUIREMENTS FOR
THE DEGREE OF
MASTER OF SCIENCE
IN
MECHANICAL ENGINEERING

By
Müge Özcan
December 2018

SMART COMPOSITES WITH TUNABLE STRESS-STRAIN CURVES
By Müge Özcan
December 2018

We certify that we have read this thesis and that in our opinion it is fully adequate, in scope and in quality, as a thesis for the degree of Master of Science.

Melih Çakmakcı(Advisor)

İlker Temizer

Yiğit Yazıcıoğlu

Approved for the Graduate School of Engineering and Science:

Ezhan Karaşan
Director of the Graduate School

ABSTRACT

SMART COMPOSITES WITH TUNABLE STRESS-STRAIN CURVES

Müge Özcan
M.S. in Mechanical Engineering
Advisor: Melih Çakmakcı
December 2018

Smart composite materials with tunable stress-strain curves are examined numerically. Microscopic constituents of the composites respond to external stimuli by changing their elastic response in a well-defined, continuous and controllable manner, which defines the tunable traits of the macroscopic constituents. This inherently dynamic behavior of the constituents results in a display of characteristic properties that cannot be attained by any combination of traditional materials. A repetitive controller, which is intrinsically fits the types of applications desired for such composites where loading is cyclic, is used to prompt microscopic adaptation of the material. Stability and performance analysis are displayed in detail for the overall numerical framework over complex paths in macroscopic stress-strain domain. Later, the feasibility of designing and analyzing smart composites for real life applications are demonstrated by incorporating the control approach within a computational setting that is based on the finite element method on representative two- and three-dimensional tunable microstructures.

Keywords: micromechanics,elactic composites, smart materials, control theory, repetitive control.

ÖZET

AYARLANILABİLİR GERİLİM-GERİNİM EĞRİLERİYLE AKILLI MALZEMELER

Müge Özcan
Makine Mühendisliği, Yüksek Lisans
Tez Danışmanı: Melih Çakmakcı
Aralık 2018

Ayarlanabilir gerilim-gerinim eğrilerine sahip akıllı kompozit malzemeler numerik olarak incelenmiştir. Bu kompozitlerin mikroskopik bileşenleri dışarıdan aldıkları uyarılara tepki vererek, makroskopik yapılarının karakteristik özelliklerini belirleyen iyi tanımlanmış, sürekli ve kontrol edilebilir bir biçimde elastik yapılarını değiştirebilirler. Bileşenlerin, doğaları gereği sergiledikleri bu dinamik davranış, geleneksel malzemelerin herhangi bir kombinasyonuyla elde edilemez. Periyodik yüklenmeye tabi tutuldukları uygulamalar göz önünde bulundurulunca, kompozitlerin sergilemesi hedeflenen makroskopik tepkiyi elde edebilmek amacıyla mikroskopik adaptasyon tekrarlamalı kontrolcü kullanılarak sağlanmıştır. Karmaşık numerik makroskopik gerilim-gerinim eğrileriden oluşan ayrıntılı örneklerle denge ve performans analizleri sergilenmiştir. Son olarak, yapılan tasarım ve analizlerin gerçek hayata uyarlanabilirliklerini test etmek amacıyla sonlu element methodu kullanılarak iki ve üç boyutlu ayarlanabilir mikro yapı örnekleri verilmiştir.

Anahtar sözcükler: mikromekanikler, elastik kompozitler, akıllı malzemeler, kontrol teorisi, tekrarlamalı kontrol.

Acknowledgement

I would like to express my immense gratitude to my supervisors Dr. Melih Çakmakcı who gave me courage when I was in despair of not being able to complete my study successfully, and Dr. İlker Temizer who improved my learning abilities with his fascinating way of thinking. I feel lucky to have studied with two supervisors who have different study areas.

During my Master's degree, I have made good friends first and then supportive colleagues. I am really grateful to meet them: Ozan Temiz who has been always on my side with his tenderness and intelligence; Mert Yüksel and Cem Kurt who have never hesitated about taking care of my well being; also Levent Dilaveroğlu, Dilara Uslu, Onur Vardar, Çağatay Karakan, Atakan Bekir Arı and Berkin Uluutku.

Most importantly, I gratefully thank my family, especially my mother Semra Özcan who supported all my educational choices, and my father Sezayi Özcan, and then Atakan Arda Nalbant who has always supported me in every way.

Contents

1 Introduction **1**

2 Mechanics in Single-Input Single-Output Settings **6**

2.1 Macroscopic Response 6

2.1.1 Average Stress Strain Relation 6

2.1.2 One-Dimensional Setting 7

2.2 Tunable Mechanics 8

2.3 Templates for Cyclic Paths in Stress-Strain Space 10

2.3.1 Macroscopic Stress and Strain Signals 10

2.3.2 Phase and Period Ratio 11

2.3.3 Signal Shape 13

2.4 Base Controller Performance 14

2.4.1 Elastic Model with Linear Control 14

2.4.2 Control Approach Alternatives 17

2.4.3 Elastic Model with Nonlinear Control 18

2.4.4 Inelastic Model 19

3 Feedback Controller Design 22

3.1 Controller Types 25

3.1.1 PI Controller 25

3.1.2 Repetitive Controller 28

4 Control in Single-Input Single-Output (SISO) Systems 34

4.1 Settings for the SISO systems 34

4.1.1 Linearization for the Nonlinear Settings 35

4.2 Control Algorithms 37

4.2.1 PI Controller 38

4.2.2 Repetitive Controller 39

4.3 Other Examples for SISO Settings 44

4.3.1 Extreme Cases 44

5 Control in Multi-Input Multi-Output (MIMO) Systems 49

5.1 Controller Design 49

5.1.1 Mathematical Modeling and Stability Analysis 50

5.1.2 Layered Composite under Biaxial Loading 52

6 FEM Based Simulations **56**

6.1 Numerical Setup 56

6.2 Two-Dimensional Mechanics 57

6.2.1 One-Variable Control (M2C1) 57

6.2.2 Two-Variable Control (M2C2) 61

6.2.3 Three-Dimensional Mechanics 63

7 Discussion **66**

List of Figures

1.1 *Microstructure design algorithms typically operate under an objective function that reflects fixed macroscale performance criteria.* 2

2.1 *Smart composite with a tunable stress-strain curve.* 9

2.2 *The influence of the period mismatch T_σ/T_ϵ and the phase θ on the cyclic stress-strain path is summarized, using cyc = cos in* (2.6). . . 12

2.3 *The influence of a triangular choice for cyc in* (2.6) *is summarized* . . 13

2.4 *The controller performance is demonstrated for the macroscopic modulus model $\overline{E}_{\|}$ from* $(2.3)_1$. 15

2.5 *For the setting of Figure 2.4, $E^{(1)}$ is varied in order to force $E^{(2)}$ towards imposed saturation limits* 16

2.6 *The controller performance is demonstrated for the macroscopic modulus model $\overline{E}_{\perp}$ from* $(2.3)_2$. 18

2.7 *Dependence of the tracking error on microscopic material properties* . 19

2.8 *Schematic representations of the inelastic model according to Generalized Maxwell element.* 20

2.9 *The controller performance is demonstrated for the case when the non-tunable constituent is viscoelastic* 21

3.1 *Feedback control system setup* 23

3.2 *Block diagram of the uncertainty model of the actuator dynamics* . . 27

3.3 *A simple repetitive control scheme* 28

3.4 *Repetitive control system representation* 29

3.5 *Equivalent system with respect to small gain theorem* 30

3.6 *Cascade compensator, or optimal state-space controller,* $C_2(s)$ *(adapted from [1])* 32

4.1 *Feedback control setup for SISO systems* 35

4.2 *Comparison of nonlinear and linearized macroscopic elastic modulus* 37

4.3 *Performance of the PI Controller (*$K_p = 133.8$, $K_i = 15168$*)* 38

4.4 *PI controller with uncertain actuators* 39

4.5 *Repetitive control scheme with proportional cascade controller* 40

4.6 *Stability analysis for different proportional gains where* $q(s) = \frac{1}{1+0.0008s}$ *and* $a(s) = 1$. 41

4.7 *Performance of the system with different feedforward functions* . . . 42

4.8 *Stability boundaries for various system delays* 45

4.9 *Performance of the repetitive control system with proportional cascade controller* 46

4.10 *Repetitive controller: full scheme* 46

4.11 *Performance of the repetitive control system with optimal state-space controller for the extreme case* $T_\sigma / T_\epsilon \to 0$. 47

4.12 *Performance of the repetitive control system with optimal state-space controller for the extreme case* $T_\sigma / T_\epsilon \to \infty$. 48

5.1 *Feedback control setup for MIMO settings* 50

5.2 *Feedback control system for layered composite model* 53

5.3 *Comparison of nonlinear and linearized microscopic elastic modulus for the MIMO case* 54

5.4 *The microstructure geometry and the loading scenario are depicted for the layered composite of Section 5.1.2.* 54

5.5 *The controller performance is demonstrated for the layered composite of Section 5.1.2.* 55

6.1 *The microstructure geometry and the loading scenario (*$\overline{\epsilon}_{12} \neq 0$*) are depicted for the M2C1 setup.* 58

6.2 *The controller performance is demonstrated for the first M2C1 setup.* 59

6.3 *The controller performance is demonstrated for the second M2C1 setup.* 60

6.4 *The microstructure geometry and the loading scenario (*$\overline{\epsilon}_{11} \neq 0$ *and* $\overline{\epsilon}_{22} \neq 0$*) are depicted for the M2C2 setup.* 61

6.5 *The controller performance is demonstrated for the M2C2 setup of Section 6.2.2.* 62

6.6 *The microstructure geometry and the loading scenario ($\overline{\epsilon}_{13} \neq 0$) are depicted for the M3C1 setup* 63

6.7 *The controller performance is demonstrated for the first M3C1 setup* 64

6.8 *The controller performance is demonstrated for the second M3C1 setup.* 65

List of Tables

4.1 *Controlled system parameters for SISO settings* 37

4.2 *System parameters for SISO models.* 44

5.1 *System parameters for layered composite model where the low pass filter* $q(s) = \frac{1}{1+0.0008s}$. 52

6.1 *System parameters for FEM-based simulations* 64

Chapter 1

Introduction

Composites have stupendous and plentiful design and performance capabilities. The earliest known application of composite materials goes back to 1500 B.C. when ancient Egyptian and Mesopotamian people mixed straw and mud together and found out that buildings made with this mixture is stronger and more durable. Their development reached its highest rate in the middle of 20th century especially with an emphasis on glass fiber reinforced composites, *fiberglass*, research [2]. They are preferred in civil, aerospace, automotive, sports and medical industries with their energy efficient, lightweight and strong structures. On the other hand, even though they have numerous options and usage areas, they cannot function any varying criteria if their constituents have *static* material properties. Their morphological or mechanical properties thus cannot evolve towards a configuration which is different from the initial design. The framework of this study is constructed around the exploration of composites which have *dynamic* properties so that they can achieve variable target behaviors.

Composites are heterogeneous materials consisting of one or more different constituents. Distrubition of the constituent(s) defines their overall mechanical behavior. In order to address desired performance criteria regarding the macroscopic response, microstructures are optimally designed to achieve

the best response under some design constraints such as volume fraction and geometry. Among many classes of composites, a widely employed class is one where major constituents are considered: *reinforcing material* and *matrix*. Reinforcing materials can be in particle or fiber form. Optimal particle morphology [3, 4] or fiber orientation [5, 6] can be achieved by a design procedure. In another class of composites, materials, including porous ones, with highly complex periodic microstructures can be manufactured in large scale by relying on novel manufacturing techniques [7]. The computational design of these complex microstructures is often realized through topology optimization techniques [8, 9], and they can also perform non-traditional macroscopic responses such as a negative thermal expansion coefficient or Poisson's ratio [10, 11, 12]. In addition, these tailored materials can meet macroscopic performance criteria such as highest stiffness at the point of application of force, structural applications can be given as an example [8, 13, 14].

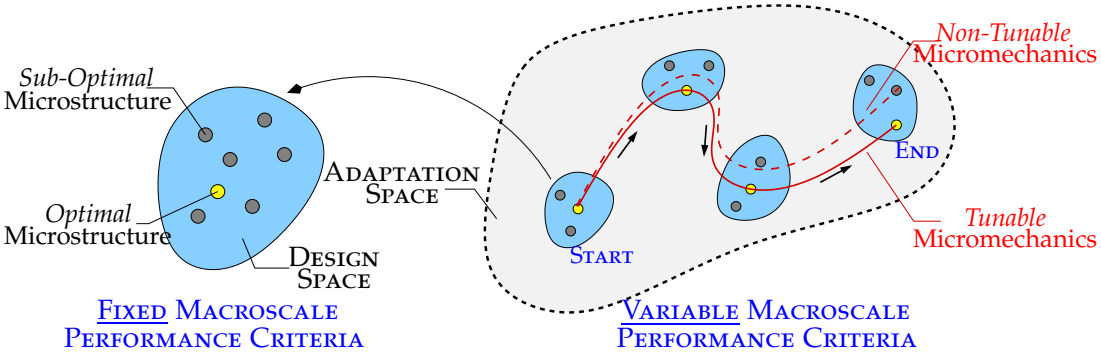

Figure 1.1: *Microstructure design algorithms typically operate under an objective function that reflects fixed macroscale performance criteria. However, the optimal design will perform increasingly sub-optimally if used under an objective function which starts with the original one and evolves towards an entirely different one. If the microstructure is additionally tunable, it can adapt to the varying performance demands in order to ensure (nearly) optimal response.*

For the fixed macroscale performance criteria, the design methodology for the composites mentioned above is considered to extract the best response possible of the optimal microstructure within the search space. However, if a design criterion changes with time, for instance the direction of the force

applied on the structure in a continuous manner, the initially optimal microstructure may be sub-optimal by the time the process ends. The microstructure needs to have the flexibility to remain optimal at all times in order to adapt to a changing criteria as depicted in Figure 1.1. To achieve this, rather than static microstructures, the dynamic ones are needed, which is the idea behind *smart* composites. It might be possible when (1) the microstructure topology or (2) the microscopic constitutive behavior can evolve in a *controllable* and *continuous* manner through an external stimulus. In this case, it can be said that the microstruture is *tunable*. It is important to underline that the dynamic behavior is needed to be controllable for the purposes of this study, in other words, a microstructural process can be activated independently from the macroscopic process which causes a change in performance criteria. For example, a microstructure can change its topology progressively with increasing load without any external stimulus [15, 16], the change is however dependent on loading, so it has no control degree of freedom. Moreover, it is important for the microstructure to respond to the stimulus continuously in order to adapt continuously to changing criteria. If the adaptation is limited to a certain degree then the topology remains fixed such as in [17], an optimal response cannot be ensured at all times. However, these examples are in the context of topology adaptation. The focus of this study is to control the path in the macroscopic stress-strain space within a purely mechanical setting.

Microstructural constituents with tunable mechanical properties, restrained to solid materials at the present, are of major importance in the context of principles discussed above. Such novel materials can respond to a variety of external stimuli in a number of different manners. Thermo-responsive materials usually have very sharp phase transitions [18], analogous to on-off switches, although some polymers with smoother phase transitions have been reported [19]. However, continuity of response and tunability of such materials remains largely inadequate in most examples to be considered in upcoming chapters. A class of responsive polymers that show promise for the purposes of this study are the magnetorheological elastomers due to the

distinct continuous effect of the magnetic field on the stress-strain curve under dynamic loading [20, 21]. Therefore, they are well-suited for utilization in tunable mechanical and structural components under cyclic loading [22, 23, 24]. There are many other novel materials that exhibit tunable characteristics that respond to stimuli such as hydration [25], photoexcitation [26], vibrational frequency [27], and pH of the environment [28]. Recently, tunable mechanical metamaterials with properties that can be controlled through different types and shapes of cuts in the material were also reported, taking the inspiration from kirigami, Japanese art of paper cutting [29]. Metamaterials in general have been gaining a lot of attention in the recent years because of their potential to be used in devices with unprecedented engineered properties [30, 31]. In addition to the examples given above, photonic crystals and auxetic metamaterials [32] have been of interest recently, due to their novel properties of controllable elastic wave propagation and having negative Poisson's ratio, respectively. As a result of their response to various external stimuli and their resulting tunable properties, controllable smart materials have a wide range of applications in tissue engineering [33], flexible electronic devices and displays [34], soft robotics [35, 36], acoustics[37], novel sensors [38, 39] just to name a few.

In order to explore the idea of tunable composites, this thesis is organized as follows. In **Chapter 2**, the micromechanical background will be given. The linear elasticity theory will be the main concern of this study. Inelastic behavior such as viscoelasticity however will be exemplified to give a demonstration of the applicability of the framework. Control of the microstructure dynamics will be achieved by using the fundamentals of feedback control theory. For this reason, feedback control systems and control methods which will be used for the control systems constitute the context of **Chapter 3**. Starting with what feedback control system is, construction of a control system and a controller will be discussed. In **Chapter 4**, according to given the micromechanical background and control methods, control systems are tested in numerical single-input single output (SISO) settings. Moreover, effects of the control system parameters on a system stability and performance will be discussed.

The extension of the ideas given in the Chapter 4 will be discussed in **Chapter 5** in numerical multi-input multi-output (MIMO) settings. Consequently, all given control methods will be performed for both various two- and three-dimensional microstructure models by using a finite element method (FEM) environment in **Chapter 6**. The aim of this chapter is to demonstrate the feasibility of attaining tunable mechanics when the microstructure is complex enough to require the computational determination of the microscopic stress field. The study is then concluded with a summary of the challenges and recommendations for future work in **Chapter 7**.

Chapter 2

Mechanics in Single-Input Single-Output Settings

2.1 Macroscopic Response

2.1.1 Average Stress Strain Relation

The macroscopic response of heterogeneous materials is obtained is typically obtained through homogenization theory [48, 49, 50, 51]. In this study, the response in macroscopic level will be estimated by focusing on the overall energy of the unit cells of periodic microstructures (see Figure 2.1), which is suitable for a homogenization-based analysis. The volume average of a unit cell is given as $\langle \mathcal{Q} \rangle = |\mathcal{Y}|^{-1} \int_{\mathcal{Y}} \mathcal{Q} \, \mathrm{d}v$, where the volume of a unit cell is $\mathcal{Y}$ and a generic, spatially variable is $\mathcal{Q}$. For a microstructure which is assumed to have M distinct constituents, each of them occupies a domain $\mathcal{Y}^{(I)} \subset \mathcal{Y}$ with a corresponding average function $\langle \mathcal{Q} \rangle^{(I)} = \left| \mathcal{Y}^{(I)} \right|^{-1} \int_{\mathcal{Y}^{(I)}} \mathcal{Q} \, \mathrm{d}v$ and a cell volume

fraction $f^{(I)} = \left|\mathcal{Y}^{(I)}\right| / |\mathcal{Y}|$. The following relation clearly also holds:

$$\langle \mathcal{Q} \rangle = \sum_{I=1}^{M} f^{(I)} \langle \mathcal{Q} \rangle^{(I)} \tag{2.1}$$

If the quantity $\mathcal{Q}$ is a constant value for each $\mathcal{Y}^{(I)}$, it can be simplified to $\langle \mathcal{Q} \rangle = \sum_I f^{(I)} \mathcal{Q}^{(I)}$.

For the *microscopic* stress (σ) and strain (ϵ) of a unit cell, with a suitable boundary condition on the unit cell for solving for their distributions through the equilibrium condition, their *macroscopic* counterparts ($\overline{\sigma}$ and $\overline{\epsilon}$) are defined as

$$\overline{\sigma} = \langle \sigma \rangle \quad , \quad \overline{\epsilon} = \langle \epsilon \rangle \tag{2.2}$$

Most of the study will be focused on an elastic response at a small deformation regime. For the linearly elastic microscopic response $\sigma(t) = \mathbb{E}\epsilon(t)$, the microscopic elasticity tensor $\mathbb{E}$ is assumed to be a constant $\mathbb{E}$ over $\mathcal{Y}^{(I)}$. The macroscopic response thus may be explicitly defined as $\overline{\sigma}(t) = \overline{\mathbb{E}}\overline{\epsilon}(t)$ where $\overline{\mathbb{E}}$ is the macroscopic elasticity tensor. In the relations, t denotes a possible time dependence which may occur because of temporal variation in the boundary conditions.

2.1.2 One-Dimensional Setting

The control system design studies will start with a SISO setting. Isotropic classical layered composite model is used for this purpose. With a uniaxial loading setup for one dimensional case, the setup is constructed parallel ($\|$) and perpendicular ($\perp$) to the loading axis of the layered composite. Macroscopic elastic modulus $\overline{E}$ which satisfies $\overline{\sigma} = \overline{E}\overline{\epsilon}$ therefore is defined in terms of the elastic moduli $E^{(I)}$ of the constituents:

$$\overline{E}_{\|} = f^{(1)}E^{(1)} + f^{(2)}E^{(2)} \quad , \quad \overline{E}_{\perp} = (f^{(1)}/E^{(1)} + f^{(2)}/E^{(2)})^{-1} \tag{2.3}$$

$\overline{E}_{\parallel}$ is a linear and $\overline{E}_{\perp}$ is a nonlinear function of the elastic modulus. As the control system framework is constructed around linear control theory in this study, $\overline{E}_{\perp}$ will help to demonstrate particular challenges. Moreover, the stress and strain will be both constants over each constituent ($\sigma^{(I)} = E^{(I)}\epsilon^{(I)}$) where $\epsilon^{(I)} = \overline{\epsilon}$ for parallel loading and $\sigma^{(I)} = \overline{\sigma}$ for perpendicular loading. In the multi-dimensional case, only the macroscopic stress $\overline{\sigma}$ will be of interest.

2.2 Tunable Mechanics

Based on the constituents in Equation 2.3, the elastic modulus of the first constituent ($E^{(1)}$) and the elastic modulus of the second one ($E^{(2)}$) will further be assumed respectively fixed and controllable. The second constituent, the controllable one, is also supposed to have a *control variable* ϕ (i.e. external stimulus to change material property), such as magnetic field for magnetorheological elastromers, so that the value of $E^{(2)}$ can be adapted between minimum and maximum values:

$$E^{(2)}_{\min} \leq E^{(2)}(\phi) \leq E^{(2)}_{\max} \quad . \tag{2.4}$$

The control variable is a function of time in practice. For the control framework of the study, the particular form of the signal $\phi(t)$ and the functional form of $E^{(2)}(\phi)$ will not be relevant. These will be considered as simplified actuator dynamics that will be discussed later. For the demonstration of the control idea, $E^{(2)}$ will be assumed as a non-decreasing function of ϕ, and therefore, the macroscopic elastic modulus $\overline{E}(\phi)$ will be a (non-decreasing) function of ϕ as well. Furthermore, when ϕ is varied together with a given strain signal $\overline{\epsilon}(t)$, the microscopic stress-strain response $\sigma^{(2)}(t) = E^{(2)}(\phi)\epsilon^{(2)}(t)$ of second constituent can follow a highly nonlinear response curve, the macroscopic response $\overline{\sigma}(t) = \overline{E}(\phi)\overline{\epsilon}(t)$ thus can have highly nonlinear response. Consequently, by adjusting the response of the control variable $\phi(t)$, the *actual* stress signal $\overline{\sigma}(t)$ can be controlled in order to follow a *target* signal $\overline{\sigma}^*(t)$. Within this control framework, $\overline{\epsilon}(t)$ is prescribed, $\phi(t)$ (or, eventually directly

$E^{(2)}(t)$) is the controlled input and $\overline{\sigma}(t)$ is the output which also defines the control error (i.e. difference between target signal and actual signal).

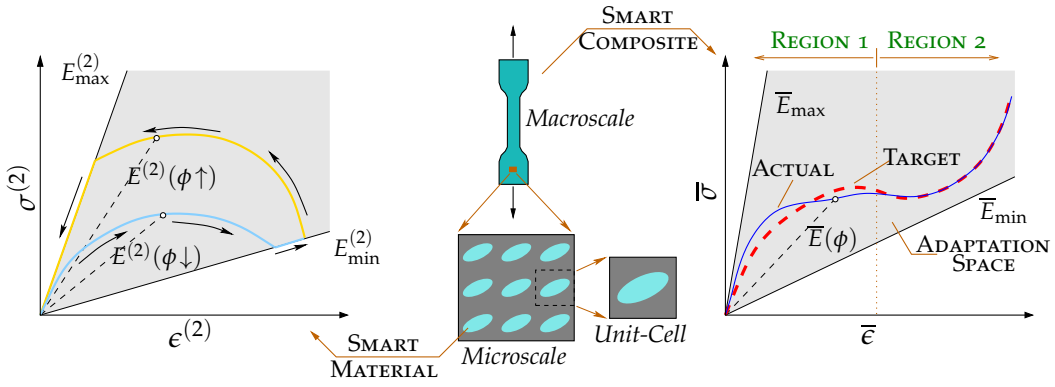

Figure 2.1: *Smart composite with a tunable stress-strain curve. The aim is to tune the elastic modulus $E^{(2)}(\phi)$ of a microscopic constituent (in this case the particle) via a control variable $\phi(t)$ so that the actual macroscopic stress $\overline{\sigma}(t)$ follows approaches a desired value $\overline{\sigma}^*(t)$ as quickly as possible and tracks this target signal with high accuracy. A numerical example which closely follows this problem depiction will be presented in Section 6.2.1.*

These ideas underline the *tunable mechanics* at the microscopic and macroscopic levels for a generic periodic microstructure as depicted in Figure 2.1. The degree of accuracy with which $\overline{\sigma}$ follows $\overline{\sigma}^*$ depends on the control system performance: the controller design and the microstructure. With a suitable control system design, it is expected that desired speed can be provided with which $\overline{\sigma}$ captures $\overline{\sigma}^*$ in a transient part (*Region 1*), and then required high accuracy of tracking of $\overline{\sigma}^*$ by $\overline{\sigma}$ is achieved in a steady-state part (*Region 2*). On the other hand, the microstructure controls the degree of freedom in the macroscopic response (*adaptation space*). As the adaptation space is characterized by the maximum ($\overline{E}_{\max}$) and minimum ($\overline{E}_{\min}$) elastic moduli, it should contain the target signal at all time in order to achieve full tracking of desired response by a proper design of the microstructure. In the upcoming sections, these aspects will be discussed.

2.3 Templates for Cyclic Paths in Stress-Strain Space

2.3.1 Macroscopic Stress and Strain Signals

Development of the control framework is based on two simplifications. First, $\overline{E}$ will be controlled directly instead of employing $\overline{E}(\phi)$ through an input $\phi(t)$. Second, The complex stress-strain paths may be obtained by changing $\overline{E}$ and $\overline{\epsilon}$ at the same time in a stress-space. As an alternative view, these complex paths may be defined by $\overline{\epsilon}(t)$ and $\overline{\sigma}^*(t)$ and they may be tracked by tuning $\overline{E}(t)$ with an appropriate control system. Both $\overline{\epsilon}(t)$ and $\overline{\sigma}^*(t)$ are defined as cyclic signals. Their phases, amplitudes, means and periods are the factors which define particular cyclic paths in the stress-strain space. These degrees of freedom in signals will be reduced by fixing the steady-state strain signal to a sinusoidal one as:

$$\overline{\epsilon}(t) = \overline{\epsilon}_o + \Delta\overline{\epsilon}\cos(2\pi t/T_\epsilon) \tag{2.5}$$

Here, $\overline{\epsilon}_o$ is fixed mean, $\Delta\overline{\epsilon}$ is fixed amplitude and T_ϵ is fixed strain period. On the other hand, the target steady-state stress signal

$$\overline{\sigma}^*(t) = \overline{\sigma}^*_o + \Delta\overline{\sigma}^*\,\mathrm{cyc}(2\pi t/T_\sigma + \theta) \tag{2.6}$$

will have variable parameters which are mean $\overline{\sigma}^*_o$, amplitude $\Delta\overline{\sigma}^*$, period T_σ and also phase θ. In the relation, *cyc* represents any cyclic signals which will be in sinusoidal or triangular shape in this study. As the stress and strain increase gradually through a short transition period in practice, target stress-strain paths are constructed with transient part as depicted in Figure 2.3. These transient parts will be assumed to be selected suitably for the controlled system.

2.3.2 Phase and Period Ratio

In this section, templates for complex cyclic stress-strain paths are provided to emphasize that how easily these complex paths can be achieved by simply changing the phase θ and the period ratio T_σ/T_ϵ. The phase between the stress and the strain signal provides damping in cyclic motion, so this parameter provides control over damping as one particular interpretation. Furthermore, the periods of the these two signals do not need to match. For instance, the macroscopic load (or, stress) can be desired to remain at a constant value whereas the macroscopic deformation (or, strain) is a cyclic signal. On the other hand, where the macroscopic loading is selected as cyclic, the macroscopic deformation can be also targeted as a constant (i.e. the motion of the object cannot be initiated unless frictional resistance overcomes). Two extreme cases, first one being $T_\sigma/T_\epsilon \to \infty$ and the second one being $T_\sigma/T_\epsilon \to 0$, and any other value between these extremes are possible from a control approach. Numerical examples for extreme cases are discussed in Section 4.3.1.

Figure 2.2 is drawn to summarize the effects of the parameters of the stress and strain signals. For the stress signal, $cyc = cos$ is chosen from Equation (2.6) and transient regions of the paths are not shown. For the first path, where $T_\sigma = T_\epsilon$ and $\theta = 0$, the path follows a straight line, which is impossible for the elastic materials with a constant $\overline{E}^* = \overline{\sigma}^*/\overline{\epsilon}$ as it does not extrapolate to the origin. The straight path is curved by adding a mismatch to the period with a zero phase, and as mismatch increases, number of inflection points increases as well. With a matching period, if a phase $\theta > 0$ is added to the signal, the straight path expands toward outside and becomes a closed cyclic path, with a clockwise direction of motion. The figure is drawn only for $\theta \leq \pi/2$. For $\theta' = \theta + \pi/2$, the path flips upside down, but the clockwise direction does not change. For $\theta' = \theta + \pi$, the path also flips upside down and the direction of motion becomes counterclockwise.

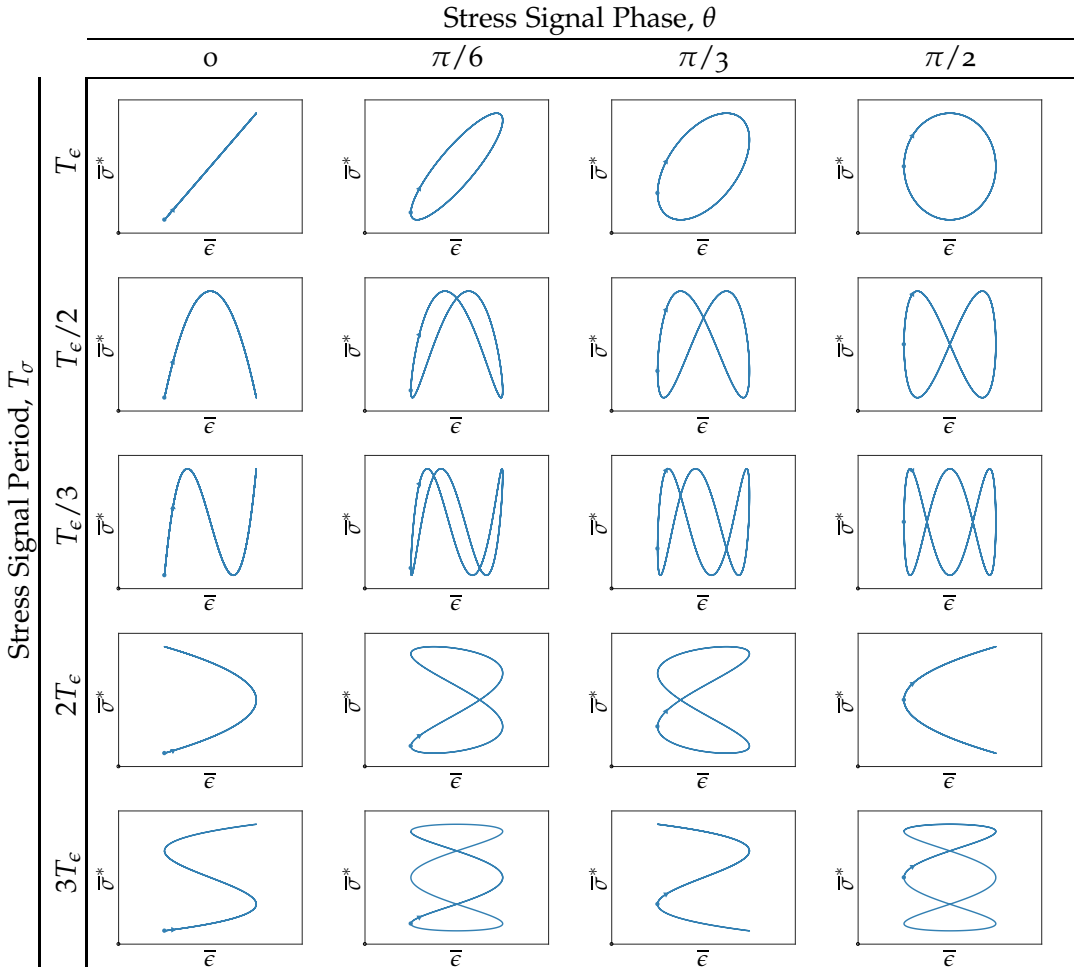

Figure 2.2: *The influence of the period mismatch T_σ/T_ϵ and the phase θ on the cyclic stress-strain path is summarized, using cyc $=$ cos in* (2.6)*. The period mismatch bends the initially straight path into a curved one while the phase splits the line into a closed path. The circle ($\circ$) at the origin indicates $(\overline{\epsilon}, \overline{\sigma}^*) = (0, 0)$, the starting point along the cyclic path is indicated with a bullet ($\bullet$) and the direction of motion is indicated with an arrow ($\blacktriangleright$).*

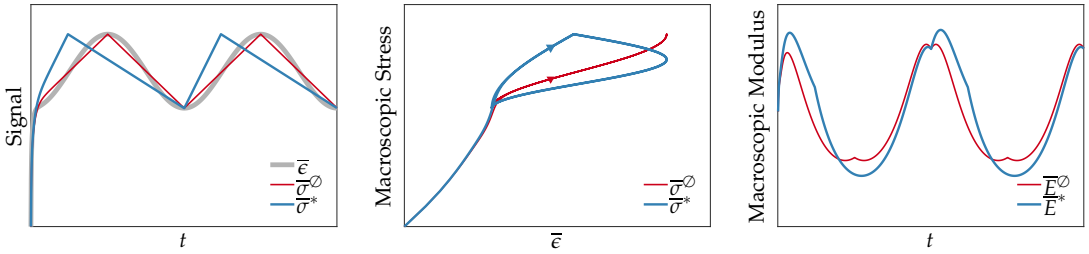

(a) Signal variations (b) Cyclic paths (c) Macrocopic moduli variations

Figure 2.3: *The influence of a triangular choice for cyc in* (2.6) *is summarized, with* $(\emptyset)$ *and without* $(*)$ *matching peaks for the stress and strain signals. The transition part of the signals are also displayed. The default target macroscopic stress will be chosen as the* $\overline{\sigma}^*(t)$ *signal shown here.*

2.3.3 Signal Shape

Another parameter for the cyclic paths is the shape of the signal. In order to demonstrate the influence of triangular choice for *cyc* in Equation (2.6) is displayed in Figure 2.3. The influence is concerned with two specific choices of the triangular signal. In the first choice, the peak values of the stress and strain signals are matched (i.e. their there is no phase shift between the peaks). However, the shapes of the signals are different from each other, a wavy shaped path is observed rather than a straight line. In the second one, the peak of the triangular shaped stress signal is shifted, the wavy shape therefore becomes a split cyclic path. This signal will be chosen as the default target macroscopic stress variation $\overline{\sigma}^*(t)$ in the SISO settings. Note that $T_\sigma = T_\epsilon$ in this choice.

Even though the difference between macroscopic modulus responses of these two choices are small, their effects on the stress-strain paths can be considered significant. Other physical parameters which affect the control system performance will be discussed later.

The macroscopic signals are assigned $\{\overline{\epsilon}_o, \Delta\overline{\epsilon}, T_\epsilon\} = \{0.02, 0.01, 5\,\mathrm{s}\}$ and

$\{\overline{\sigma}_o, \Delta\overline{\sigma}\} = \{1.05\,\text{MPa}, 0.25\,\text{MPa}\}$. Moreover, $E^{(1)} = 50\,\text{MPa}$ and $f^{(1)} = f^{(2)} = 0.5$ unless otherwise noted. Finally, the particular value of the period of the signals, T_ϵ, will not be important for this study since its influence on macroscopic response will be defined according to material properties and other dynamics in the control system. Hence, the variation of the control quantities will be monitored by using number of cycles instead of the system time.

2.4 Base Controller Performance

2.4.1 Elastic Model with Linear Control

Among the macroscopic moduli of (2.3), $\overline{E}_{\parallel}$ is linear whereas $\overline{E}_{\perp}$ is nonlinear where $E^{(2)}$ is a tunable macroscopic modulus. The linear model will be held in first step to assess the controller performance. The *tracking error* (Σ) is defined by evaluating the control error in the immediate past over a duration of one period:

$$\Sigma(t) = \left(\frac{1}{T_\sigma} \int_{t-T_\sigma}^{t} \left(\frac{\overline{\sigma} - \overline{\sigma}^*}{\overline{\sigma}^*} \right)^2 \, \mathrm{d}t \right)^{1/2} \tag{2.7}$$

In a MIMO setting, the notation Σ_{ij} will be defined for the particular stress component $\overline{\sigma}_{ij}$.

The base controller performance for this one-dimensional linear setting is given in Figure 2.4. It can be clearly seen that the macroscopic actual response tracks the target signal. The criteria for a suitable performance is decided with respect to tracking error value after 15 cycles. This performance criterion is set for less than one percent deviation from the target signal.

As previously discussed in Section 2.2 and demonstrated in Figure 2.1, there may be limits for the range in which $E^{(2)}$ may be varied. In Figure 2.5, the behavior of the base controller is shown under these limitations. $E^{(1)}$ is decreased to 35 MPa from 50 MPa as its default value, so that $E^{(2)}$ requires

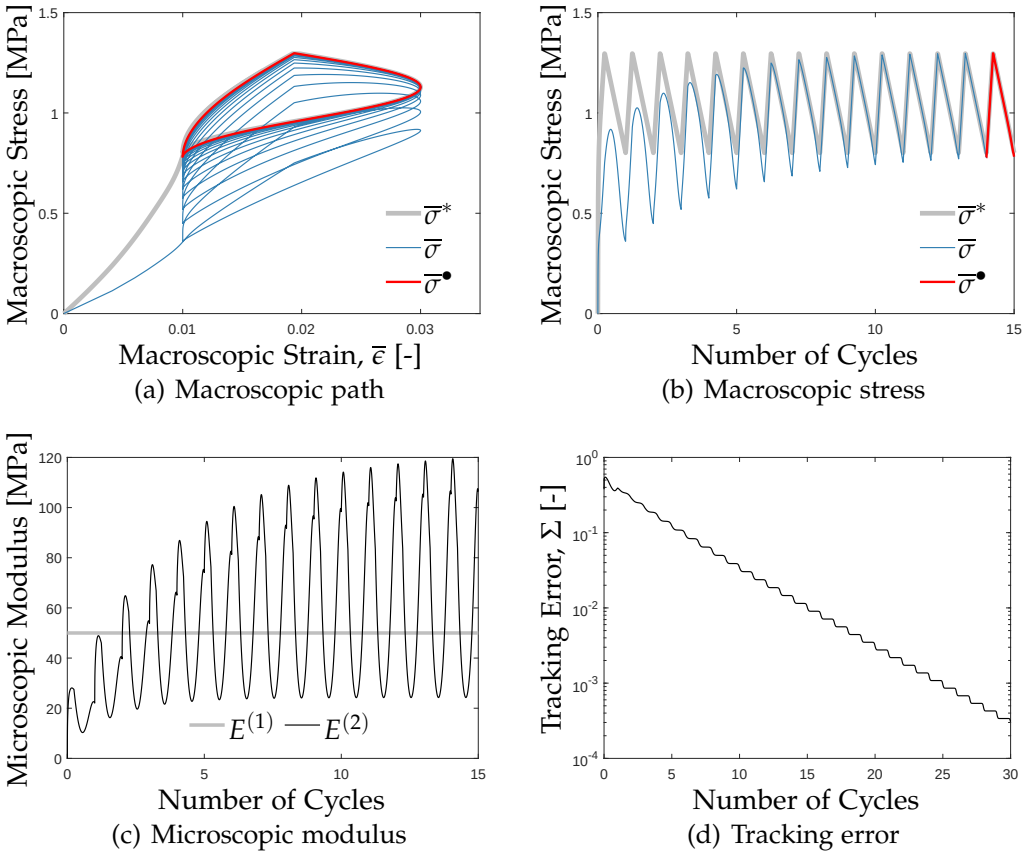

Figure 2.4: *The controller performance is demonstrated for the macroscopic modulus model* $\overline{E}_{\parallel}$ *from* $(2.3)_1$. *The tracking error from* (2.7) *decreases below one percent after 15 cycles. The* $\overline{\sigma}$ *signal over this cycle and its path in the macroscopic stress-strain space is indicated with the* $\overline{\sigma}^\bullet$ *curve.*

larger values in order to achieve the desired macroscopic modulus. Therefore, if $E^{(2)}_{\max} = 120\,\text{MPa}$ is imposed, $E^{(2)}$ saturates at this value. It also limits $\overline{E}$ to a maximum value $\overline{E}_{\max}$ and, consequently, $\overline{\sigma}$ to $\overline{\sigma}_{\max} = \overline{E}_{\max}\overline{\epsilon}$. At this maximum saturation limit, a constant modulus response is observed. For the minimum saturation limit, a similar saturation effect may be observed. For example, using $E^{(1)} = 75\,\text{MPa}$, $E^{(2)}$ is limited to $E^{(2)}_{\min} = 10\,\text{MPa}$, and then $\overline{\sigma}$ is limited to $\overline{\sigma}_{\min} = \overline{E}_{\min}\overline{\epsilon}$. In practice, even though the controller may be capable of giving a suitable response at saturation limits, saturation limits of the microstructures can be checked as a pre-processing stage to get possible best response from the tunable material.

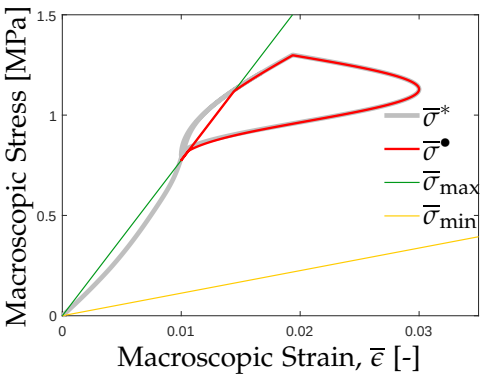

(a-1) Macroscopic path with *max*-saturation

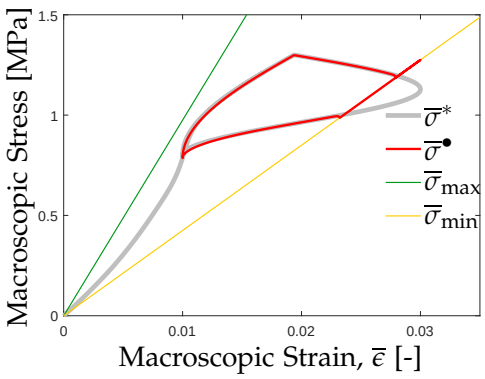

(b-1) Macroscopic path with *min*-saturation

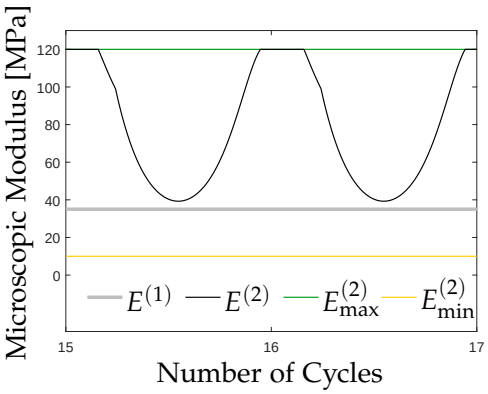

(a-2) Microscopic modulus with *max*-saturation

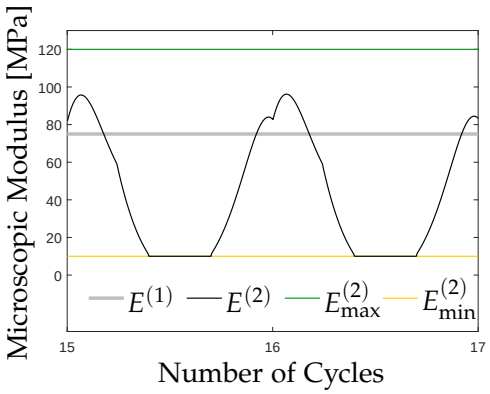

(b-2) Microscopic modulus with *min*-saturation

Figure 2.5: *For the setting of Figure 2.4, $E^{(1)}$ is varied in order to force $E^{(2)}$ towards imposed saturation limits $E^{(2)}_{\max} = 120\,MPa$ and $E^{(2)}_{\min} = 10\,MPa$. For case (a), $E^{(1)} = 35\,MPa$ for which $\overline{E}_{\max} = 77.5\,MPa$ and $\overline{E}_{\min} = 22.5\,MPa$, leading to max-saturation. For case (b), $E^{(1)} = 75\,MPa$ for which $\overline{E}_{\max} = 97.5\,MPa$ and $\overline{E}_{\min} = 42.5\,MPa$, leading to min-saturation. The macroscopic stress $\overline{\sigma}$ saturates to either $\overline{\sigma}_{\max} = \overline{E}_{\max}\overline{\epsilon}$ or $\overline{\sigma}_{\min} = \overline{E}_{\min}\overline{\epsilon}$ type response.*

2.4.2 Control Approach Alternatives

In the particular setting of the previous section, the value of $E^{(2)}$ can be easily calculated from $(2.3)_1$. $\overline{E}$ thus matches the desired value $\overline{E}^* = \overline{\sigma}^*/\overline{\epsilon}$ without the need for a control approach. At this stage, it is beneficial to deviate from the numerical investigations and highlight two remarkable advantages of the approach over such an alternative:

1. *Computational complexity:* It is not always easy to achieve desired macroscopic modulus by optimizing a microscopic one especially in a multi-dimensional case as stated previously. It may require solving multiple cell problems of homogenization with iterative optimization techniques. As at each time step, same iterations are needed to find a solution, it will be excessively expensive. The control approach on the other hand carries out a similar optimization but essentially on the fly. Consequently, the behavior in the transient period is possibly suboptimal but the long term behavior is of very high accuracy, which is achieved at a much lower cost.

2. *Microscopic uncertainty:* The macroscopic response is characterized through microscopic response with a set of assumptions which can be easily violated in practice. These assumptions can be, for instance, purely elastic microscopic mechanical response, precisely known microscopic elastic moduli and microstructure topology. In practice, uncertain microscopic mechanical behavior or lack of knowledge on properties will always lead to an error while characterizing the macroscopic response. On the other hand, a desired stress strain path can be achieved by controlling the tunable constituent of the microstructure, whether or not the microscopic behavior is known exactly. This is essentially due to the fact that tuning remains active as long as the target is not matched.

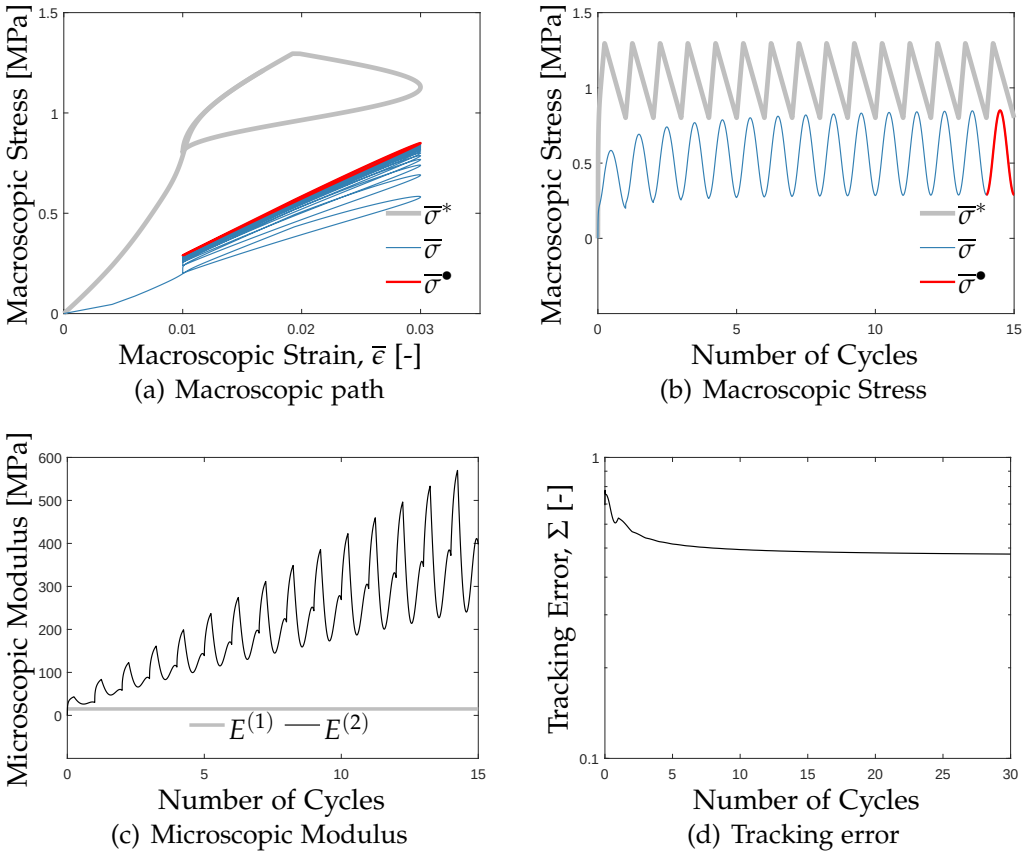

(a) Macroscopic path (b) Macroscopic Stress (c) Microscopic Modulus (d) Tracking error

Figure 2.6: *The controller performance is demonstrated for the macroscopic modulus model $\overline{E}_\perp$ from $(2.3)_2$. The target path is unrealizable due to the micstructure topology, leading to a saturating tracking error even if a continous increase in $E^{(2)}$ is allowed.*

2.4.3 Elastic Model with Nonlinear Control

To emphasize the importance of the microstructure topology on control capacity, the nonlinear macroscopic modulus $\overline{E}_\perp$ of $(2.3)_2$ will be considered with default parameters except for the new choice $E^{(1)} = 15\,\text{MPa}$. With this parameter selection, even though $E^{(2)}$ goes to infinity, macrostructure response cannot track the target signal and the tracking error saturates to an undesired limit as depicted in Figure 2.6. The reason of the saturation in the macroscopic space is the limited influence of $E^{(2)}$ even if it goes to infinity. The model $\overline{E}_\perp$ is therefore limited to a finite value. Consequently, this finite value

is too low so that the target path lies outside of the adaptation space. If the microstructure topology limits the tracking of the signal, and the error cannot be set to zero, the target path will be referred to as *unrealizable*.

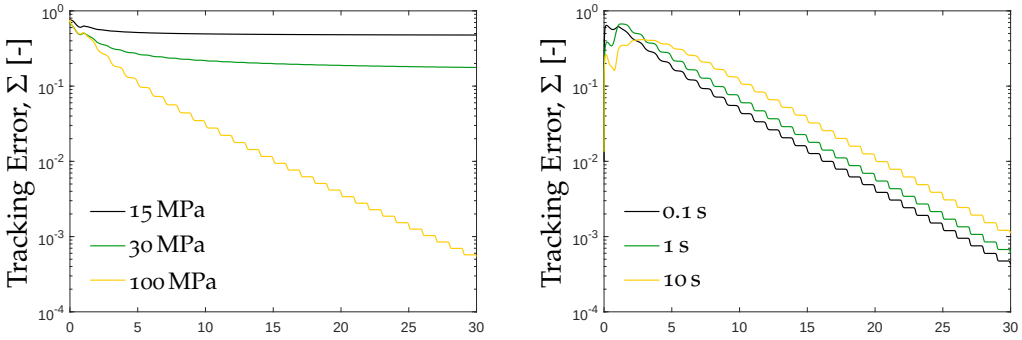

(a) Tracking error for different $E^{(1)}$ (b) Tracking error for different τ

Figure 2.7: *Dependence of the tracking error on microscopic material properties: (a) $E^{(1)}$ is varied when the macroscopic response is described by $\overline{E}_{\perp}$ from $(2.3)_2$, eventually delivering a realizable response when $E^{(1)}$ is sufficiently large, and (b) the relaxation time is varied beyond the period $T_\sigma = 5\,s$ for the case with a non-tunable viscoelastic constituent.*

2.4.4 Inelastic Model

Inelastic response of the constituents leads to a nonlinear macroscopic mechanical response as well. As an example, one may consider the case where the tunable constituent is still elastic but non-tunable constituent of $(2.3)_2$ will be viscoelastic, therefore macroscopic response is viscoelastic, in order to demonstrate the performance of the base controller. Macroscopic stress response $\overline{\sigma} = f^{(1)}\sigma^{(1)} + f^{(2)}\sigma^{(2)}$ will be calculated via (2.1) where strain is constant over both constituents. The tunable constituent has thus $\sigma^{(2)} = E^{(2)}\overline{\epsilon}$. The viscoelastic constituent is modeled with the standard linear solid $\sigma^{(1)} = \sigma_e^{(1)} + \sigma_v^{(1)}$ with $\sigma_e^{(1)} = E_\infty^{(1)}\overline{\epsilon}$ and $\sigma_v^{(2)} = E_v^{(1)}(\overline{\epsilon} - \epsilon_v)$. The overall composite behavior closely represents the generalized Maxwell element model of viscoelasticity, as depicted in Figure 2.8. The rate of the microscopic

viscous strain ϵ_v is governed by the equation $\tau\dot{\epsilon}_v + \epsilon_v = \overline{\epsilon}$ where τ is the relaxation time, and it comes from $\tau = \eta / E_v^{(1)}$ where η is viscosity. $E_\infty^{(1)} = 100\,\text{MPa}$ and $E_v^{(1)} = 10\,\text{MPa}$ will be considered. For $\tau = 1\,\text{s}$, the controller performance is depicted in Figure 2.9. $\overline{\sigma}$ takes negative values in the early stages of loading because of viscoelasticity. Furthermore, the macroscopic stress-strain path displays hysteresis as the relaxation time is very close to $T_\sigma = 5\,\text{s}$. It shows that the controller is also working against this hysteresis to track the target stress signal, and it is weakly influenced by the relaxation time. Figure 2.7(b) shows that the target path is effectively achieved in comparable times even if τ significantly changes, and even when it is larger than T_σ.

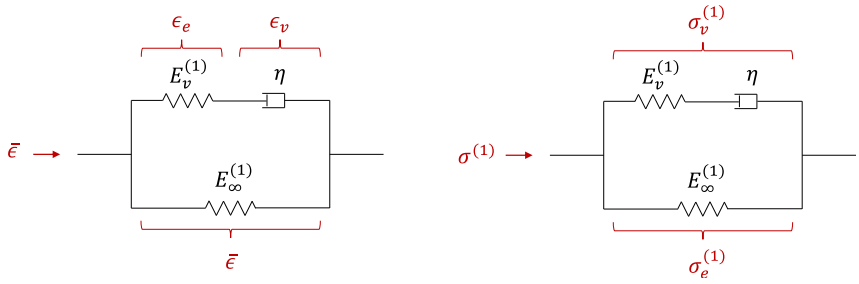

(a) Generalized Maxwell element

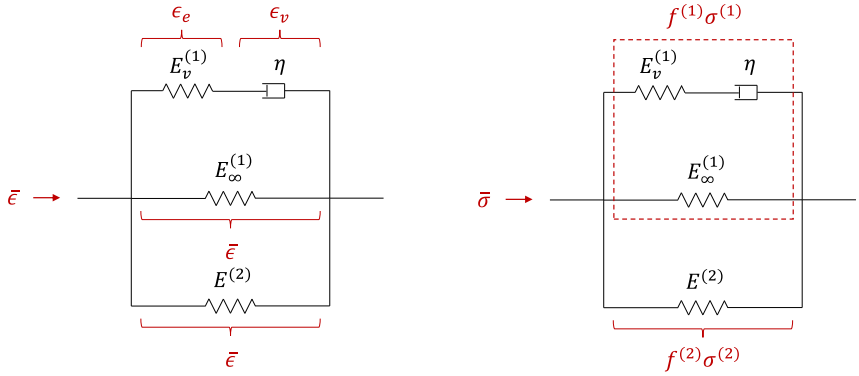

(b) Schematic representation of the inelastic model

Figure 2.8: *Schematic representations of the inelastic model according to Generalized Maxwell element.*

In this chapter, mechanics aspects and physical challenges which are associated with the control of tunable composites were underlined. For this purpose, the base controller was employed. A detailed examination of this

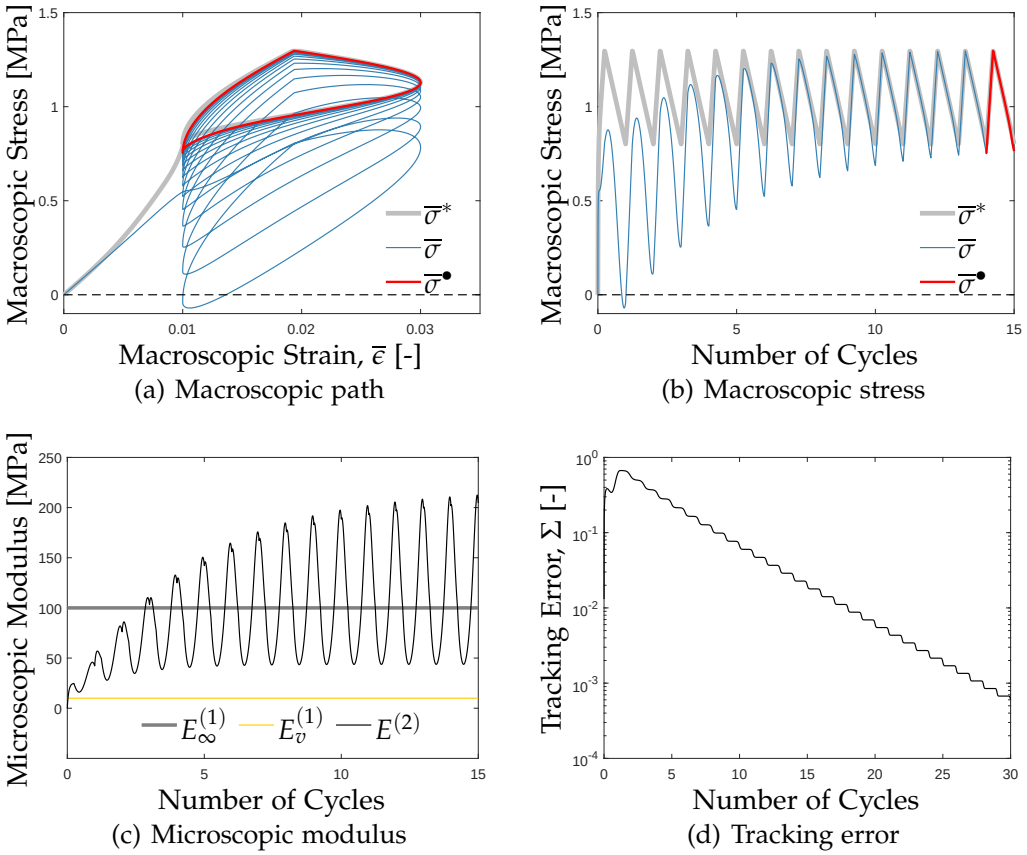

(a) Macroscopic path (b) Macroscopic stress (c) Microscopic modulus (d) Tracking error

Figure 2.9: *The controller performance is demonstrated for the case when the non-tunable constituent is viscoelastic, characterized by the material parameters* $\{E_\infty^{(1)}, E_v^{(1)}, \tau\}$*, with* $\tau = 1\,s$.

controller and its further development will be carried out in the following chapters.

Chapter 3

Feedback Controller Design

Devices and algorithms that are added to a process to regulate its output are known as control systems. In a typical setup, controller which houses the algorithm, receives the reference input and system output measurement from the sensor. The reference input generally indicates the desired value of the process (controlled system, $F(s)$) output. Using the comparison of its inputs controller calculates the command to be sent to the actuator of the plant as shown in Figure 3.1(a).

In real life, there are various non-ideal factors that affect the operation of the system. In Figure 3.1(b), $H(s)$ represent the dynamics of the sensor that provides the feedback information to the controller in as a transfer function and $A(s)$ represents the dynamics associated with the actuator component of the system in Laplace domain. Both actuator and sensor dynamics can be as simple as a time delay or saturation or more complicated dynamics such as flexibility. The portion of the system that includes all of the actuators, sensor and process dynamics is known as the *plant* model $P(s)$. In some cases the output of the plant is affected by disturbance inputs whose effect can be represented as an additive or multiplicative operation as shown in Figure 3.1(b). In this study, feedback control systems will be assumed to have perfect sensor dynamics (i.e. $H(s) \equiv 1$) and no noise. The actuator dynamics

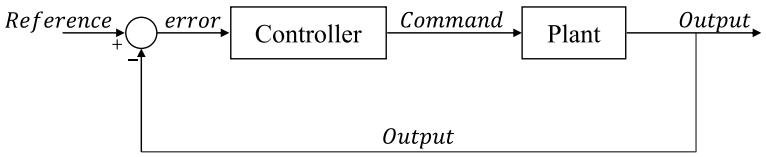

(a) Ideal

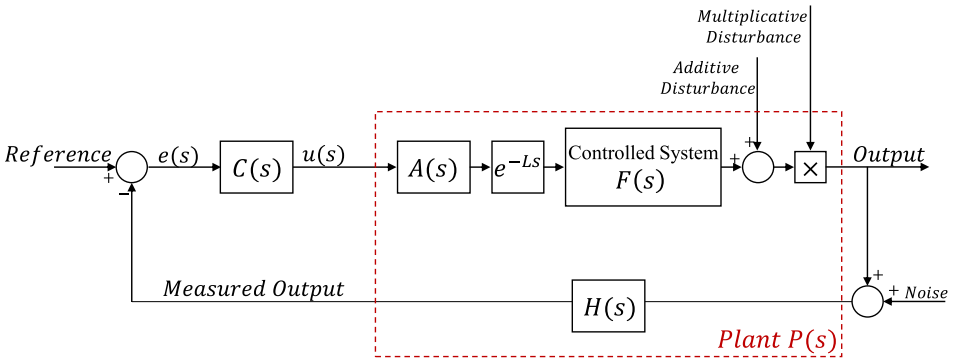

(b) Non-ideal

Figure 3.1: *Feedback control system setup*

will represent actuator inertia, the actuator function $A(s)$ will be taken in the form of low pass filter:

$$A(s) = \frac{1}{as + 1} \tag{3.1}$$

In order to design a control system with desirable performance, it has to present four important qualities:

- The control system should be *stable*. A stable system has bounded output signal when its input signal is bounded, or a system is stable if it tends to return back its equilibrium point when it is perturbed. Instability of a system can be result of a unstable plant dynamics, or of a poorly designed control system.

- The control system should display good *tracking* performance. It is achieved when the actual output signal can follow the desired output signal within tolerable limits.
- The control system should *reject disturbances*. Additive disturbances threaten boundedness of the signal and the amount of tracking error, whereas multiplicative ones can change the behavior of the system.
- The control system should be *robust* enough to withstand to modeling errors and plant changes.

Controller design techniques can be divided into two categories: *classical* and *modern* control methods. Classical methods use Laplace transform for continuous systems and z-transform for discrete systems. Its main advantage is that differential equations of the dynamic responses in time domain can be transformed into algebraic equations in frequency domain so that computational cost decreases. For a dynamic system, the transformation formulation is

$$F(s) = \int_{-\infty}^{\infty} f(t)e^{-st}dt \tag{3.2}$$

where $f(t)$ is a time dependent function of the system, $F(s)$ is s function in Laplace domain. On the other hand, modern control methods use state-space representation of ODE which provides handling of the systems that have more than one input or output signals with ease. Standard form of the state-space representation is

$$\begin{aligned} \dot{x}(t) &= Ax(t) + Bu(t) \\ y(t) &= Cx(t) + Du(t) \end{aligned} \tag{3.3}$$

where $x(t)$ is the state vector, $\dot{x}(t)$ is derivative of the state vector, $u(t)$ is control input vector, and $y(t)$ is the output vector. A is the system matrix which represents internal dynamics of the system, B is the input matrix. System outputs are calculated by using the output matrix C and the feedforward matrix D [40]. In this study, both techniques will be used to design control systems depending on the system needs and requirements.

Next, Proportional and Integral (PI) control and repetitive control concepts will be given. The control systems, will be designed with these controllers, and their performances will be discussed.

3.1 Controller Types

3.1.1 PI Controller

A typical controller algorithm for the system represented in Figure 3.1(b) can be given as the proportional-integral control (PI) algorithm. This algorithm uses the current error of the system $e(t)$ and calculates the command $u(t)$ to be send to the actuator based on history and the current value of the error as shown in 3.4.

$$u(t) = K_p e(t) + K_i \int_0^t e(t)dt \tag{3.4}$$

where constants K_p and K_i are the so-called proportional and integral controller constants respectively. Best performance from the system can be obtained by adjusting (tuning) these constants. Control algorithms can be represented as in linear operations using their Laplace form. In the case of the PI controller, the controller transfer function is

$$C(s) = \frac{u(s)}{e(s)} = K_p + \frac{K_i}{s} \tag{3.5}$$

where $e(s)$ and $u(s)$ are Laplace transform of $e(t)$ and $u(t)$ shown in Figure 3.1(b).

3.1.1.1 Uncertainty Modeling and Stability

Model variations or uncertainty in a system may be the reason of instability. There are several methods in literature for designing stable controllers for

plants with uncertainties [41]. For example from the present system, the parameter a can be considered as an uncertain parameter between $[0.001, 0.01]$. The actuator function with uncertainty then becomes

$$\widetilde{A}(s) = \frac{1}{as+1} \tag{3.6}$$

where $\widetilde{A}(s)$ is called as perturbed actuator function. For design and analysis of the system, nominal plant $A(s)$ of $\widetilde{A}(s)$ is needed. To calculate this nominal function, uncertainty of $\widetilde{A}(s)$ will be modeled as a function of $A(s)$:

$$\widetilde{A}(s) = \frac{A(s)}{1+\Delta W(s)A(s)} \tag{3.7}$$

where $W(s)$ a weighting transfer function, and Δ is corresponding perturbation between $[-1, 1]$. For $A(s) = \frac{1}{a_n s+1}$, (3.7) can be rewritten as

$$\widetilde{A}(s) = \frac{1}{a_n s+1+\Delta W(s)} \tag{3.8}$$

and $as + 1 = a_n s + 1 + \Delta W(s)$, so that $as = a_n s + \Delta W(s)$. When $\Delta = -1$, $a = 0.001$ and $a_n - W(s)/s = 0.001$, whereas when $\Delta = 1$, $a = 0.01$ and $a_n + W(s)/s = 0.01$. Therefore, $a_n = 0.0055$ and $W(s) = 0.0045s$. Consequently, the nominal plant becomes

$$A(s) = \frac{1}{0.0055s+1} \tag{3.9}$$

Block diagram representation of the perturbed plant using the uncertainty formulation is shown in Figure 3.2. Note that, in the rest of the study, the actuator function will be assumed as the transfer function given in 3.9.

Stability analysis of the systems with uncertain parameters is in the scope of robust control field and studied by many researchers [42, 43, 44, 45]. By the small gain theorem [46], which will be detailed though repetitive controllers, H_∞ norm analysis of the system is beheld for the stability. Using the

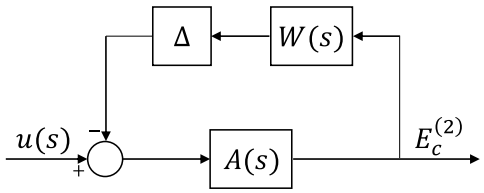

Figure 3.2: *Block diagram of the uncertainty model of the actuator dynamics*

uncertainty model is 3.7, the stability analysis required

$$\|WPS\|_\infty < 1 \tag{3.10}$$

where S is the sensitivity function. The sensitivity function S of a feedback control system provides information about the effect of feedback loop on the output signal. For the setup such in Figure 3.1(b), a sensitivity function is determined as

$$S(s) = \frac{1}{1 + P(s)C(s)} \tag{3.11}$$

Uncertainty of the plant is studied during the design on PI controller in the next chapters.

3.1.1.2 PI Controller Design in MIMO systems

A system has has multiple inputs multiple outputs is called a multi-input multi-output (MIMO) system. For a MIMO system, controlled system is a matrix $\mathbf{F}(s)$ with nxn terms for n number of inputs and n number of outputs. For a traditional controller such as PI controller, the controller design is done for each loop of the system, that is n controllers are designed for the controlled system. However, because of the interaction among the feedback loops, the controller may lead to instability of the system. As a remedy, the system can be decoupled (i.e. eliminating the coupled terms of the system plant) [47].

Decoupling method for a $2x2$ system with plant $\mathbf{P}(s)$ can be given as

$$\underbrace{\begin{bmatrix} P_{d1}(s) & 0 \\ 0 & P_{d2}(s) \end{bmatrix}}_{\mathbf{P}_d(s)} = \underbrace{\begin{bmatrix} P_{11}(s) & P_{12}(s) \\ P_{21}(s) & P_{22}(s) \end{bmatrix}}_{\mathbf{P}(s)} \underbrace{\begin{bmatrix} 1 & D_{12}(s) \\ D_{21}(s) & 1 \end{bmatrix}}_{\mathbf{D}(s)} \tag{3.12}$$

where $\mathbf{P}_d(s)$ is decoupled plant, and $\mathbf{D}(s)$ is decoupling matrix. Two PI controllers can be designed for the decoupled plant $\mathbf{P}_d(s)$. Therefore, the controllers do not interact as the controlled loops are separated from each other.

3.1.2 Repetitive Controller

Repetitive control is used for control systems which have fixed periodic reference inputs. Control inputs of the systems are calculated by using error of the previous period. This feature provides a simple learning ability to the control scheme. Figure 3.3 shows the repetitive control idea: e^{-Ts} gives one period delay (i.e. T seconds) to the error signal.

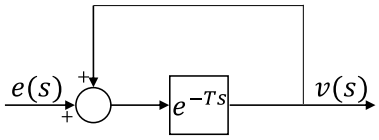

Figure 3.3: *A simple repetitive control scheme*

Figure 3.4 shows the repetitive control system which is introduced by Hara et al. [1]. The compensated plant $G(s)$ is constructed with an additional control structure $C_2(s)$ and the plant model $P(s)$. $C_1(s)$ is the transfer function of the repetitive controller. $C(s) = C_2(s)C_1(s)$ gives the overall controller of the system which represented in Figure 3.1(b).

A simple repetitive controller scheme given in Figure 3.3 is modified as in Figure 3.4 with addition of $q(s)$ a *low pass filter* and a proper transfer function

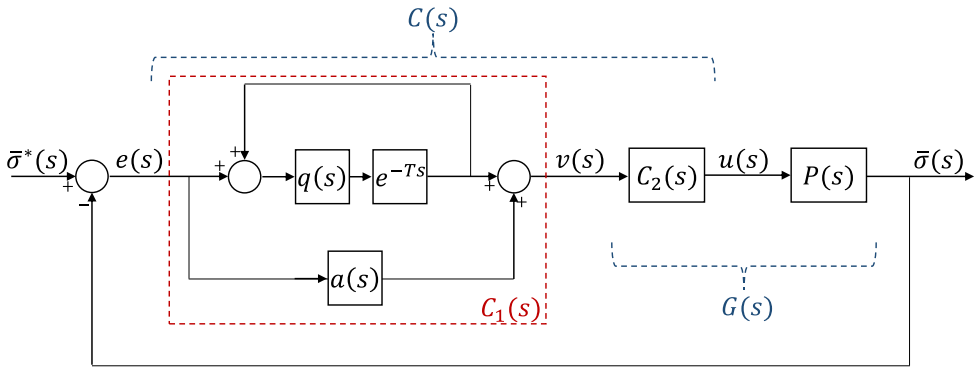

Figure 3.4: *Repetitive control system representation*

$a(s)$. $C_1(s)$ thus becomes

$$C_1(s) = a(s) + \frac{q(s)e^{-Ts}}{1 - q(s)e^{-Ts}} \tag{3.13}$$

The additional controller $C_2(s)$ can be any controller that satisfies the stability criterion. Hara defines it with two different approaches: *state-space approach* and *factorization approach*. In this study, $C_2(s)$ will be first a proportional gain K_p. Then a Kalman filter with a quadratic regulator will be used $C_2(s)$ by using state-space approach.

3.1.2.1 Stability Analysis of Repetitive Controller

Stability analysis of a repetitive control system is a H_∞ control problem which originates from the small gain theorem. Small gain theorem states that the system will be stable if the norm of the overall system or the open loop system is smaller than unity for all frequency values [46]. An equivalent version of the system is therefore constructed to eliminate time delay term of the controller e^{-Ts} from the stability analysis. Using the system shown in Figure 3.4, the error and the output can be derived as $e(s) = R(s) - Y(s)$ and $Y(s) = G(s)C_1(s)e(s)$. When these equations and $C_1(s)$ from (3.13) are reformulated,

with $q(s) \equiv 1$, the equivalent system is defined as

$$\begin{aligned} e(s) &= (I + a(s)G(s))^{-1}(1 - e^{-Ts})R(s) \\ &\quad + (I + a(s)G(s))^{-1}(I + (a(s) - 1)G(s))e^{-Ts}e(s) \end{aligned} \tag{3.14}$$

and from this relation

$$\mathscr{L}^{-1}\{(1 - e^{-Ts})R(s)\} = r(t) - r(t - T) \tag{3.15}$$

The reference input $r(t)$ is periodic and bounded. Where the period of $r(t)$ is T_r, $r(t) = r(t - T_r)$ for $t \geq T_r$. (3.15) becomes 0 when system time (t) is larger than the system period. However, if it is less than the period, the inverse Laplace is equal to $r(t)$. In this case, it follows from the reference input and the error relation, $(I + a(s)G(s))^{-1}G(s))$ is assumed to be proper rational stable transfer function (i.e. its all pole in the left hand plane, denoted by $\mathbb{R}_{-}(s)$). With this assumption, the equivalent system is obtained as shown in Figure 3.5.

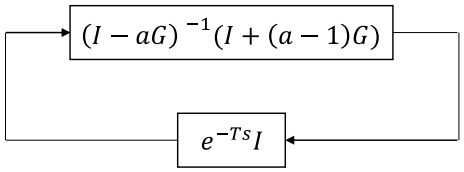

Figure 3.5: *Equivalent system with respect to small gain theorem*

Small gain theorem proposes that H_∞ norm of the connected stable systems on the loop should be less than 1 for stability:

$$\left\|(I + aG)^{-1}(I + (a - 1)G)\right\|_\infty \cdot \left\|e^{-Ts}\right\|_\infty < 1 \tag{3.16}$$

as $\left\|e^{-Ts}\right\|_\infty = 1$, the condition becomes

$$\left\|(I + aG)^{-1}(I + (a - 1)G)\right\|_\infty < 1 \tag{3.17}$$

If the reference signal contains high frequency modes such as very sharp edges, tracking might become unattainable. In order to achieve tracking by decreasing the loop gain of the controller in high frequency range, a low pass filter is introduced to the system. Moreover, a system with time delay may lead to exponential increase in magnitude of frequency domain, the low pass filter will help to keep the system stable. Until this point (while discussing the stability analysis of the repetitive controller), the low pass filter in Figure 3.4 was assumed to be $q(s) \equiv 1$, meaning that there was no low pass filter. From now on, it will be included in the system with a proper transfer function, so $\left\| q(s)(I + aG)^{-1}(I + (a-1)G) \right\|_\infty < 1$ is determined as the new stability condition. Therefore, a repetitive control system is stable if it meets the following criteria

$$1. \quad (I + a(s)G(s))^{-1})G(s) \in \mathbb{R}_-(s) \tag{3.18}$$

$$2. \quad \left\| q(s)(I + aG)^{-1}(I + (a-1)G) \right\|_\infty < 1 \tag{3.19}$$

Low pass filter affects the tracking performance and stability. If amplitude of the filter is close to 0 in low frequency range (i.e. the frequencies that are less than cutoff frequency ω_c of the system), tracking becomes difficult. For the best tracking performance, the amplitude should be close to 1 in this range. In high frequency range, if the amplitude is close to 0, stability increases. Hence, the filter should have some frequency characteristics:

$$q(j\omega) = \begin{cases} \sim 1 & \mid \omega \mid \leq \omega_c \\ < 1 & \mid \omega \mid > \omega_c \end{cases} \tag{3.20}$$

3.1.2.2 Optimal State-Space Controller Design by Synthesis Algorithm

The synthesis algorithm is constructed for minimum phase systems by using Kalman filter and perfect regulation methods. For $a(s) = 1$, stability relation

is

$$\left\| q(s)(I + G(s))^{-1} \right\|_{\infty} < 1 \tag{3.21}$$

If the given system contains any state which cannot be controlled from the input or cannot be observed from the output, it is called uncontrollable or unobservable. Before the construction of a cascade compensator $C(s)$, this system should be made both controllable and observable by eliminating these states. This procedure is called minimal realization or minimal-dimensional, and it provides minimum dimension for the state-space equation [40]. A minimal realization of the given plant $P(s)$ can be represented as

$$P(s) = C_p(sI - A_p)^{-1}B_p \tag{3.22}$$

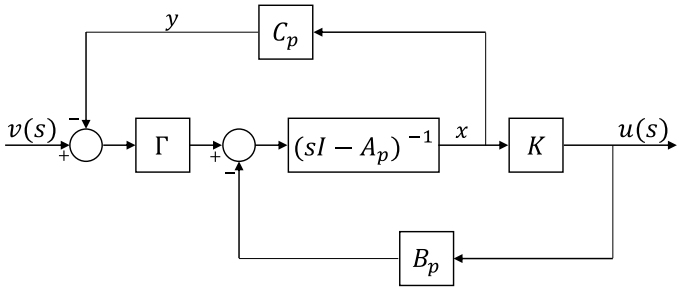

Figure 3.6: *Cascade compensator, or optimal state-space controller, $C_2(s)$ (adapted from [1])*

Cascade compensator $C_2(s)$ is structured as shown in Figure 3.6: Γ represents the Kalman filter gain, and K is the gain of perfect regulation. Γ is calculated from a positive definite solution of Algebraic Riccati Equation (ARE):

$$A_p X + X{A_p}^T + \Phi - X{C_p}^T C_p X = 0 \tag{3.23}$$

where X is the positive definite solution and the gain is

$$\Gamma = X{C_p}^T \tag{3.24}$$

for controllable $(A_p, \Phi^{1/2})$ pair. Note that showing observability is not necessary for positive definite stabilizing solution of ARE [45].

The gain K is a optimal solution of linear quadratic regulator (LQR) problem. The input function $u(t)$ is a function of estimated state $\dot{x}$ of the system where $u(t) = Kx(t)$. By solving the LQR problem, the cost function (i.e. quadratic performance index) shown in (3.25) is minimized:

$$J = \int_0^\infty (x^T Q x + u^T R u) dt \tag{3.25}$$

where Q and R are some positive definite weighting matrices. This cost function is minimized by using the solution of the ARE given in (3.26).

$$A_p Y + Y{A_p}^T + Q - Y B_p R^{-1} B_p^T Y = 0 \tag{3.26}$$

Once the solution to ARE is found the controller gain can be calculated as

$$K = R^{-1} B_p^T Y \tag{3.27}$$

Chapter 4

Control in Single-Input Single-Output (SISO) Systems

In Chapter 3, an overview of feedback control systems and detailed information about controller types which will be used were discussed. In this chapter, design and analysis of the control systems for SISO systems will be discussed.

4.1 Settings for the SISO systems

In order to design and analyze the performance of a control system, the mathematical representation of the controlled system $F(s)$ and of the plant $P(s)$ are needed. By using the proposed one-dimensional settings in Section 2.1.2, a feedback control setup for a linear relationship of macroscopic elastic modulus in terms of the controlled microscopic elastic modulus ${E_c}^{(2)}$ is structured as in Figure 4.1 according to Figure 3.1(b). The linear relationship from 2.3_1 is

$$\overline{E}_{\parallel}(t) = E^{(1)}(t)f^{(1)} + {E_c}^{(2)}(t)f^{(2)} \tag{4.1}$$

Using 4.1 it can be concluded that the controlled system becomes $F(s) = f^{(2)}$. The behavior of the non-controlled constituent $E^{(1)}(t)f^{(1)}$ is assumed to be additive disturbance, and the macroscopic strain function $\overline{\epsilon}(t)$ is a multiplicative disturbance as shown in Figure 4.1. Note that the controlled microscopic modulus will be denoted with $(\cdot)_c$ in the following discussions.

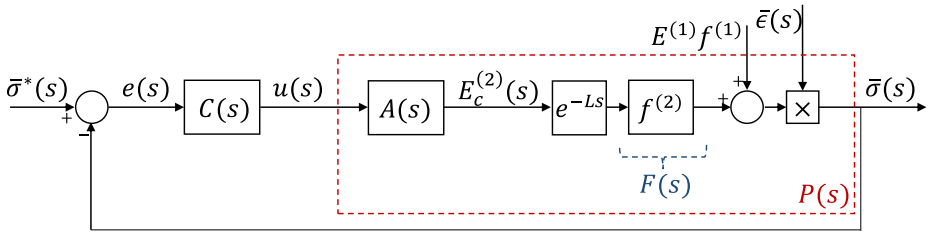

Figure 4.1: *Feedback control setup for SISO systems*

The cyclic strain function causes nonlinearity in the system. For the stability analyses, in order to avoid complexity, its maximum gain effect on the system is denoted as $\widehat{\epsilon} = \max_{0<t} \epsilon(t)$. The plant model for the SISO settings therefore can be represented as

$$P(s) = \widehat{\epsilon} e^{-Ls} F(s) A(s) \tag{4.2}$$

where $A(s)$ the actuator dynamics given in 3.1.1.1 and e^{-Ls} is the time delay of the system.

4.1.1 Linearization for the Nonlinear Settings

Mathematical representation of the controlled system should be linear in order to use the low order controller methods as in proposed in this study. On the other hand, for most detailed model representations such as the expression given in $(2.3)_2$, the perpendicular macroscopic elastic modulus is

nonlinear:

$$\overline{E}_{\perp}(t) = \frac{E^{(1)}(t){E_c}^{(2)}(t)}{E^{(1)}(t)f^{(1)} + {E_c}^{(2)}(t)f^{(2)}} \tag{4.3}$$

In this case, an approximated controlled system model can be obtained by linearizing the nonlinear relation in (4.3) using Taylor expansion as:

$$\begin{aligned}\overline{E}_{\perp}(t) &\approx \overline{E}_{\perp}(t_0) + \frac{\partial \overline{E}_{\perp}}{\partial E^{(1)}}(E^{(1)}(t) - E^{(1)}(t_0)) + \frac{\partial \overline{E}_{\perp}}{\partial {E_c}^{(2)}}({E_c}^{(2)}(t) - {E_c}^{(2)}(t_0)) \\ &= \frac{{{E_c}^{(2)}}^2(t_0)f^{(1)}}{(E^{(1)}(t_0)f^{(2)} + {E_c}^{(2)}(t_0)f^{(1)})^2}E^{(1)}(t) \\ &\quad + \frac{{E^{(1)}}^2(t_0)f^{(2)}}{(E^{(1)}(t_0)f^{(2)} + {E_c}^{(2)}(t_0)f^{(1)})^2}{E_c}^{(2)}(t)\end{aligned} \tag{4.4}$$

t_0 indicates the time in which the relation is linearized. By replacing the constant portions of the relationship above with constants ${f^{(1)}}^*$ and ${f^{(2)}}^*$, a simpler controlled system model can be formulated as

$$\overline{E}_{\perp}(t) \approx E^{(1)}(t){f^{(1)}}^* + {E_c}^{(2)}(t){f^{(2)}}^* \tag{4.5}$$

For instance, after linearizing (4.5) around the operating points $E^{(1)}(t_0) = 100\text{MPa}$ and $E^{(2)}(t_0) = 58.30\text{MPa}$ the simpler model is validated against the nonlinear version as shown in Figure 4.2, indicating a very good match between nonlinear and linearized macroscopic elastic modulus signal. According to these points, model parameters can be given as ${f^{(1)}}^* = 0.2713$ and ${f^{(2)}}^* = 0.7981$.

In the following section, analysis and performances of the control algorithms for various cases, such as time delay and uncertainty, will be discussed. Parameters of controlled systems which will be used in the control algorithms in this chapter will be as in Table 4.1.

Recall from Section 2.1.2, the linear $\overline{E}_{\perp}$ and nonlinear $\overline{E}_{\parallel}$ relationships are for the same microstructure, i.e. *laminar composite*. Linearity or nonlinearity of the relation is defined with respect to loading direction.

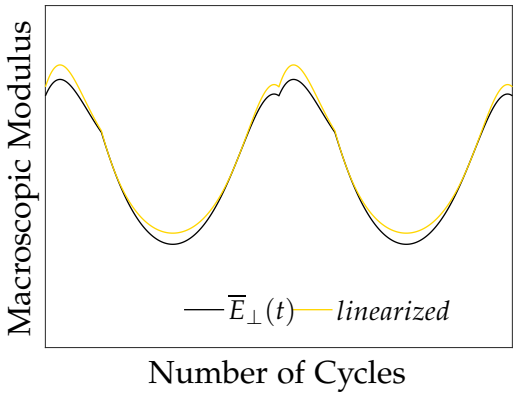

Figure 4.2: *Comparison of nonlinear and linearized macroscopic elastic modulus*

Model	Fraction	$F(s)$	$E^{(1)}$	$\widehat{\epsilon}$
Linear ($\overline{E}_{\parallel}$)	$f^{(1)} = f^{(2)} = 0.5$	$f^{(2)} = 0.5$	50MPa	0.003
Nonlinear ($\overline{E}_{\perp}$)	$f^{(1)} = f^{(2)} = 0.5$	$f^{(2)^*} = 0.7981$	50MPa	0.003

Table 4.1: *Controlled system parameters for SISO settings*

4.2 Control Algorithms

In Figure 4.1, block diagram representation of control systems for SISO setting was given. $\overline{\sigma}^*(s)$ and $\overline{\sigma}(s)$ are frequency domain representations of the reference input signal $\overline{\sigma}^*(t)$ and the actual output signal $\overline{\sigma}(t)$, respectively. As stated in Chapter 3, $C(s)$ is an error based feedback controller, $A(s) = \frac{1}{0.0055s+1}$ is the actuator, and e^{-Ls} is time delay term of the actuator. Unless otherwise stated, time delay for the actuator is taken 0.0005 seconds, (i.e. $L = 0.0005$).

4.2.1 PI Controller

The controller parameters K_p and K_i of PI control (see 3.5) are tuned to find an optimal controller performance. For constants $K_p = 133.8$ and $K_i = 15168$, the control system performance is given in Figure 4.3.

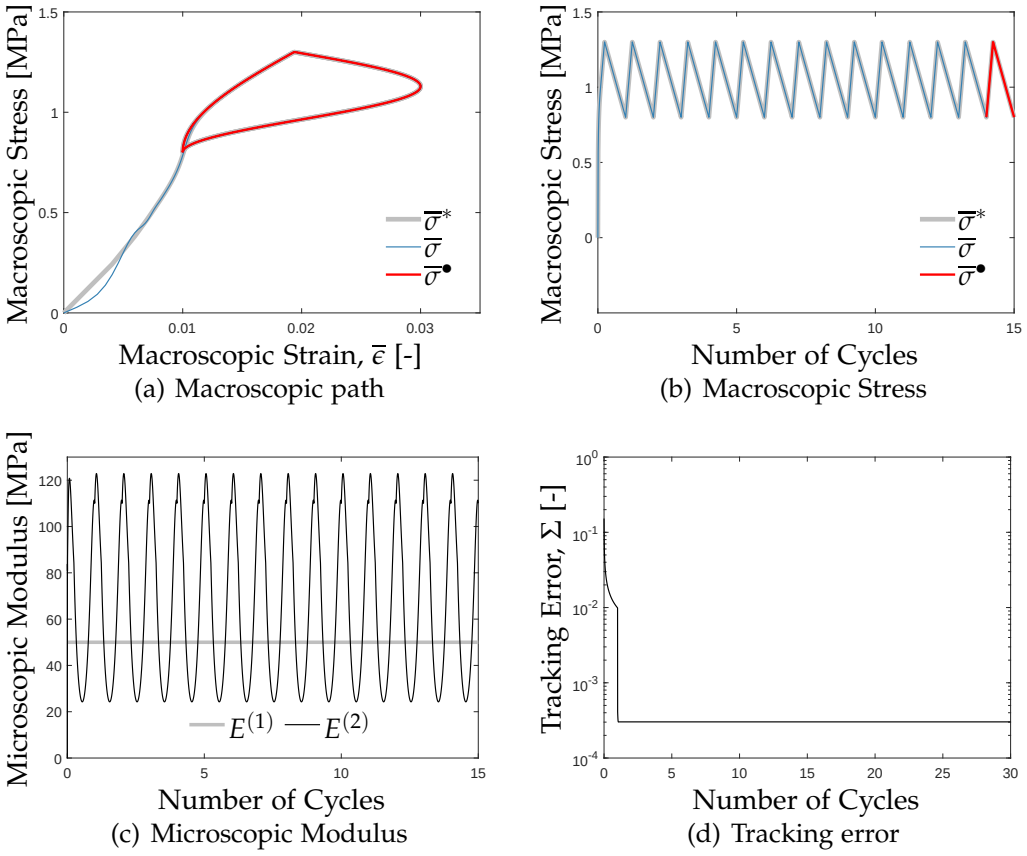

(a) Macroscopic path (b) Macroscopic Stress (c) Microscopic Modulus (d) Tracking error

Figure 4.3: *Performance of the PI Controller ($K_p = 133.8$, $K_i = 15168$)*

4.2.1.1 Stability Analysis for Uncertainty

In Section 3.1.1.1, an uncertainty model is constructed for the uncertain parameter a of the actuator: $\widetilde{A}(s) = \frac{A(s)}{1+\Delta W(s)A(s)}$ (see also 3.7). According to stability analysis $\|WPS\|_\infty < 1$, the norm is calculated as 0.0123 for $K_p = 133.8$

and $K_i = 15168$. The result shows that the system is robust for uncertain parameter a between $[0.001, 0.01]$. In Figure 4.4, the tracking error performance of the controller for the actuator plant models $A_u(s)$ and $A_l(s)$ is depicted.

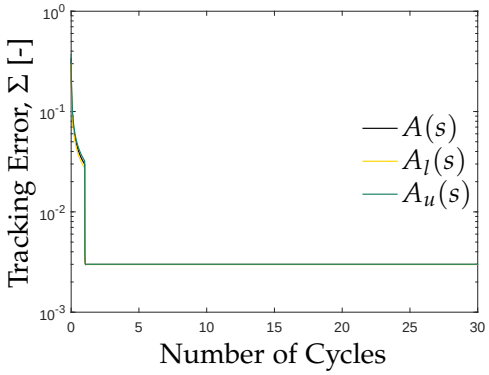

Figure 4.4: *PI controller with uncertain actuators:* $A(s) = \frac{1}{0.0055s+1}$*, for the lower bound of* $a = 0.001$ *the actuator is* $A_l(s) = \frac{1}{0.001s+1}$*, for the upper bound of* $a = 0.01$ *the actuator is* $A_u(s) = \frac{1}{0.01s+1}$

4.2.2 Repetitive Controller

Repetitive control methods are discussed in Section 3.1.2. Here, its implementation to one-dimensional settings will be demonstrated. Consequently, from (3.19), stability condition for SISO settings becomes

$$\left\| (1 + a(s)G(s))^{-1}(1 + (a(s) - 1)G(s)) \right\|_\infty < 1 \tag{4.6}$$

where $(1 + a(s)G(s))^{-1}G(s) \in \mathbb{R}_-(s)$ from 3.18.

4.2.2.1 Repetitive Control with Proportional Cascade Controller

A repetitive control system has two controller parts: repetitive controller and cascade controller. In Figure 4.5, repetitive control scheme is represented for cascade controller is selected as proportional gain. In this section, impact

of the control system parameters on the system performance, as well as the performances of the SISO microstructure settings will be discussed.

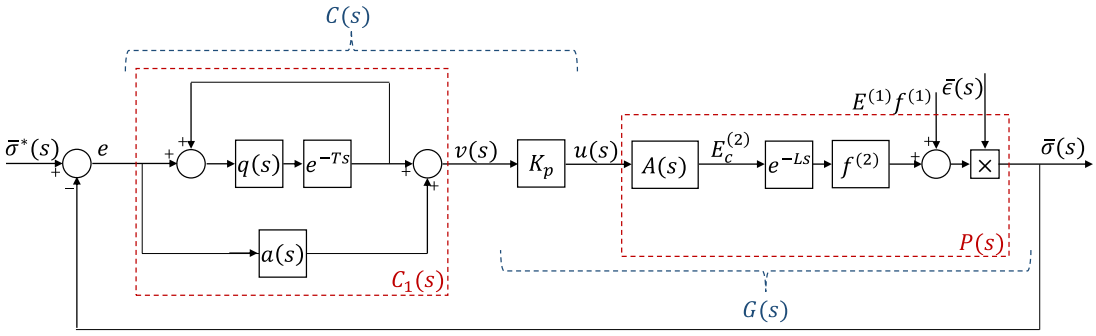

Figure 4.5: *Repetitive control scheme with proportional cascade controller*

Proportional gain K_p selection:

As discussed in Chapter 2, it is already discussed that the control system is stable if the H_∞ norm of the system is less than unity. However, in some cases, although this condition is satisfied, the system may be unstable as the output signal of the system increases without bounds. To avoid this situation, it is important to observe the phase part of the Bode plot. For example, in Figure 4.6, Bode plots of a setting for $K_p = 100$ and $K_p = 2000$ are given. The stability results for both systems imply that they are stable as their maximum absolute magnitudes are less than unity. However, the system with $K_p = 2000$ is made is observed to be unstable. The cause for its instability is the reversal of its phase angle to positive values at high frequencies, which in turn increases the tracking error.

Rational function $a(s)$ selection:

The feedforward loop of the repetitive controller $C_1(s)$ has the rational function $a(s)$. To show the possible effects of this function, it is selected as unity

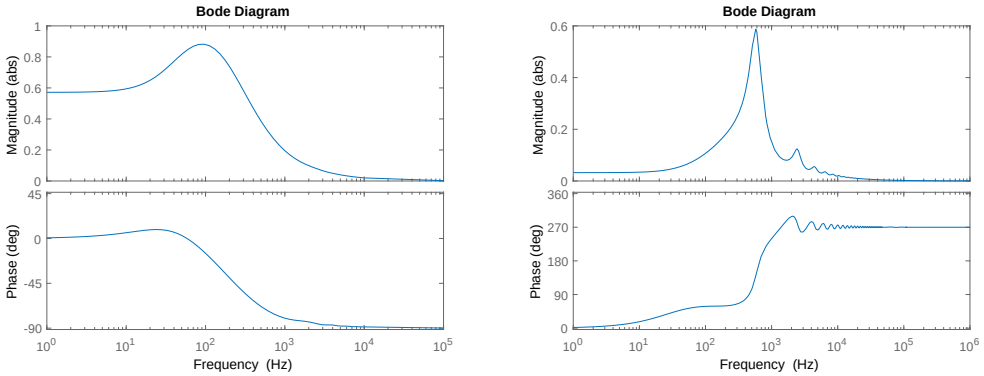

(a) $K_p = 100$ (b) $K_p = 2000$

Figure 4.6: *Stability analysis for different proportional gains where* $q(s) = \frac{1}{1+0.0008s}$ *and* $a(s) = 1$. *Phase plots give a clue about stability rather than magnitude plots.*

gain, lag and lead compensator, and the other parameter of the controller $q(s)$ is selected with a lower cut-off frequency which leads to poor tracking performance of the output signal. $q(s)$ is purposefully selected as to decrease the tracking performance of the system in order to analyze the effect of the feedforward loop on the overall performance of the system. The lag compensator slows down the system but at the end it decreases the tracking error to a small amount, whereas lead compensator speeds up the system but increases the tracking error as also shown with the results given in Figure 4.7.

Effect of the Actuator Delay time L:

Nearly all systems display time delay effects due to the nature of its sensing and actuation components. In this study, it is assumed that the system delay L comes from the actuator dynamics. Amount of time delay has a huge impact on the system performance. It is not straight forward to examine this effect while analyzing the system as it adds infinite poles on the imaginary axis. Pade approximation and uncertainty modeling of the delay term e^{-Ls} are some of the methods to obtain a simple function of the delay term to use

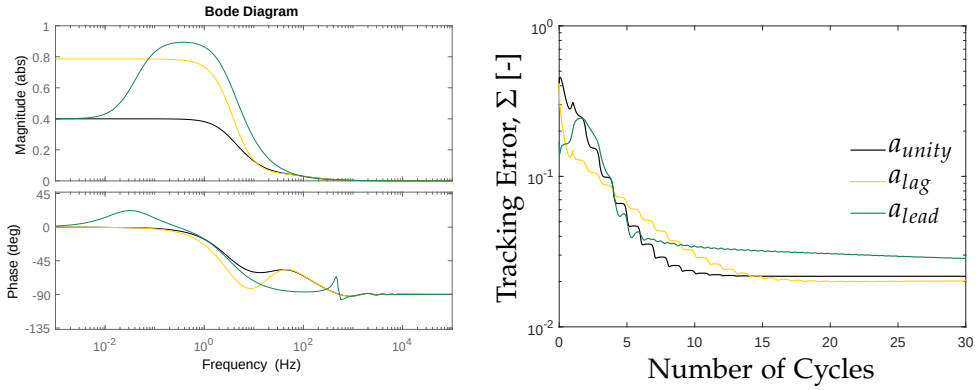

(a) (b)

Figure 4.7: *Performance of the system with different feedforward functions:* $a_{unity}(s) = 1$,$a_{lag}(s) = \frac{1+0.025s}{0.25(1+0.1s)}$,*and* $a_{lead}(s) = \frac{1+5s}{1+0.5s}$ *where* $q(s) = \frac{1}{1+0.05s}$ *and* $K_p = 100$

in further analysis. However, in this study, rather than using a method to simplify it, all systems are considered to have no time delay first. Later, at the last step of the analysis, Bode plot of the system is performed with time delay term and if needed the control parameters are changed.

In Figure 4.8, for different time delays, Bode plots of the systems are shown. Proportional gain K_p and low-pass filter $q(s)$ are modified according to time delay. Note that these diagrams do not promise a good tracking. Even though the systems are within the stability boundaries, large time delay decreases the tracking performance.

Low-pass filter $q(s)$ selection:

In section 3.1.2.1, it was stated that low-pass filter needs to have some frequency characteristics for optimal tracking and stability results. Keeping all other system parameters the same (i.e. $K_p = 100$ and $a(s) = 1$), for well selected and poorly selected cut-off frequency of $q(s)$ steady-state tracking errors are 0.00037 as shown in Figure 4.9 and 0.02 as shown in Figure 4.7.

4.2.2.2 Repetitive Control with Optimal State-Space Controller

For the design of the optimal controller, first, the proper feedforward function is taken as $a(s) = 1$, and $C_2(s)$ is assumed as Kalman filter with perfect regulator. The full block diagram of this control system is depicted in Figure 4.10.

In Section 3.1.2.2 the development of the controller is given with detailed information. The design steps can be outlined as:

1. Find a minimum realization for the plant without actuator delay term $\widetilde{P}(s)$,
2. By using the minimal realization parameters of the plant, find a positive definite solution X of Algebraic Riccati Equation (ARE) for a suitable observer weight Φ: $A_p X + X{A_p}^T + \Phi - X{C_p}^T C_p X = 0$
3. Calculate the gain of Kalman filter: $\Gamma = X{C_p}^T$,
4. To find an optimal gain K, by minimizing the cost function J by another ARE for some positive definite Q and R values: $A_p Y + Y{A_p}^T + Q - Y B_p R^{-1} B_p^T Y = 0$,
5. Find the gain K using $K = R^{-1}{B_p}^T Y$.

For both the linear and nonlinear model, weighting factors are selected as $\Phi = \sqrt{20000}$, $R = 1$ and $Q = 10^6$. According to these values, the control system parameters are tabulated in Table 4.2.

Model	$\widetilde{P}(s)$	Γ	K	$\|\cdot\|_\infty$	Filter $q(s)$
Linear ($\overline{E}_{\|}$)	$0.03\frac{0.5}{1+0.0055s}$	61.03	913.21	0.98	$\frac{1}{1+0.0008s}$
Nonlinear ($\overline{E}_{\perp}$)	$0.03\frac{0.7981}{1+0.0055s}$	80.72	913.21	0.99	$\frac{1}{1+0.0008s}$

Table 4.2: *System parameters for SISO models.*

4.3 Other Examples for SISO Settings

4.3.1 Extreme Cases

It is almost impossible to follow some complex stress-strain paths if the macrostructure has fixed material properties. In Section 2.3.2, two extreme cases are used as examples of these cases. The first case is cyclic macroscopic deformation under constant loading, whereas the latter case is cyclic loading where there is no deformation. Even though they are difficult to achieve with static macrostructures, it becomes trivial if the macrostructure has dynamic constituents. For the linear SISO control setting, these extreme models are demonstrated and they are depicted in Figure 4.11 and Figure 4.12.

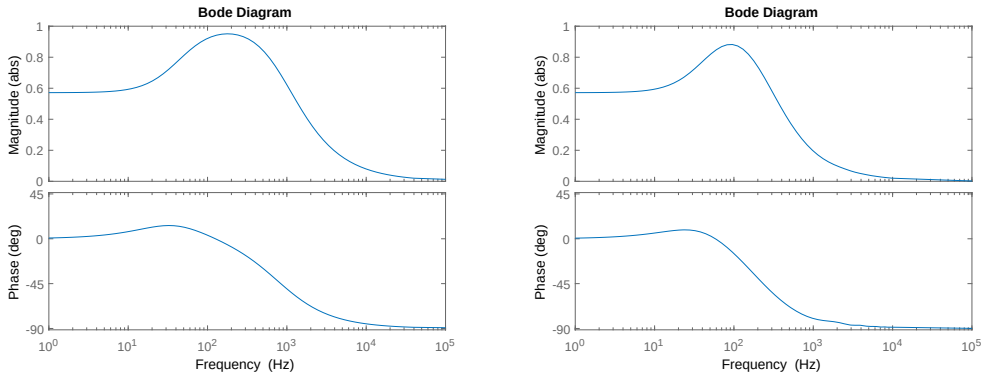

(a)

(b)

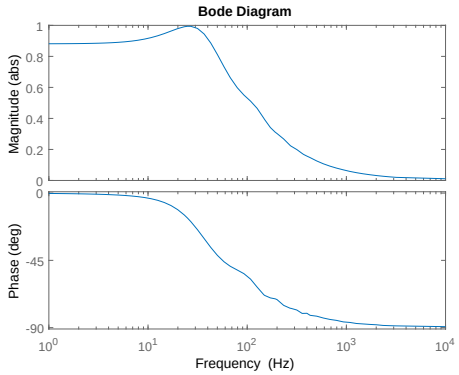

(c)

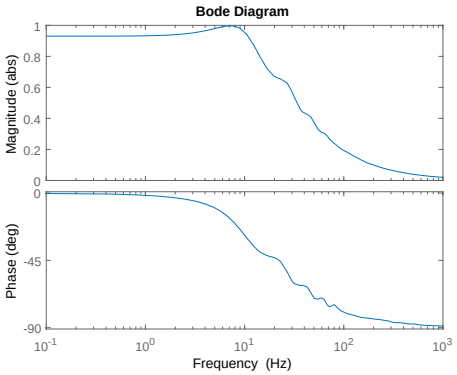

(d)

Figure 4.8: *Stability boundaries for various system delays: (a)* $L = 0(nodelay)$, $K_p = 100$, $\| \cdot \|_\infty = 0.923$, $q(s) = \frac{1}{1+0.0002s}$,*(b)* $L = 0.0005sec$, $K_p = 100$, $\| \cdot \|_\infty = 0.844$, $q(s) = \frac{1}{1+0.0008s}$,*(c)* $L = 0.01sec$, $K_p = 20$, $\| \cdot \|_\infty = 0.981$, $q(s) = \frac{1}{1+0.004s}$, *and (d)* $L = 0.05sec$, $K_p = 5$, $\| \cdot \|_\infty = 0.996$, $q(s) = \frac{1}{1+0.008s}$

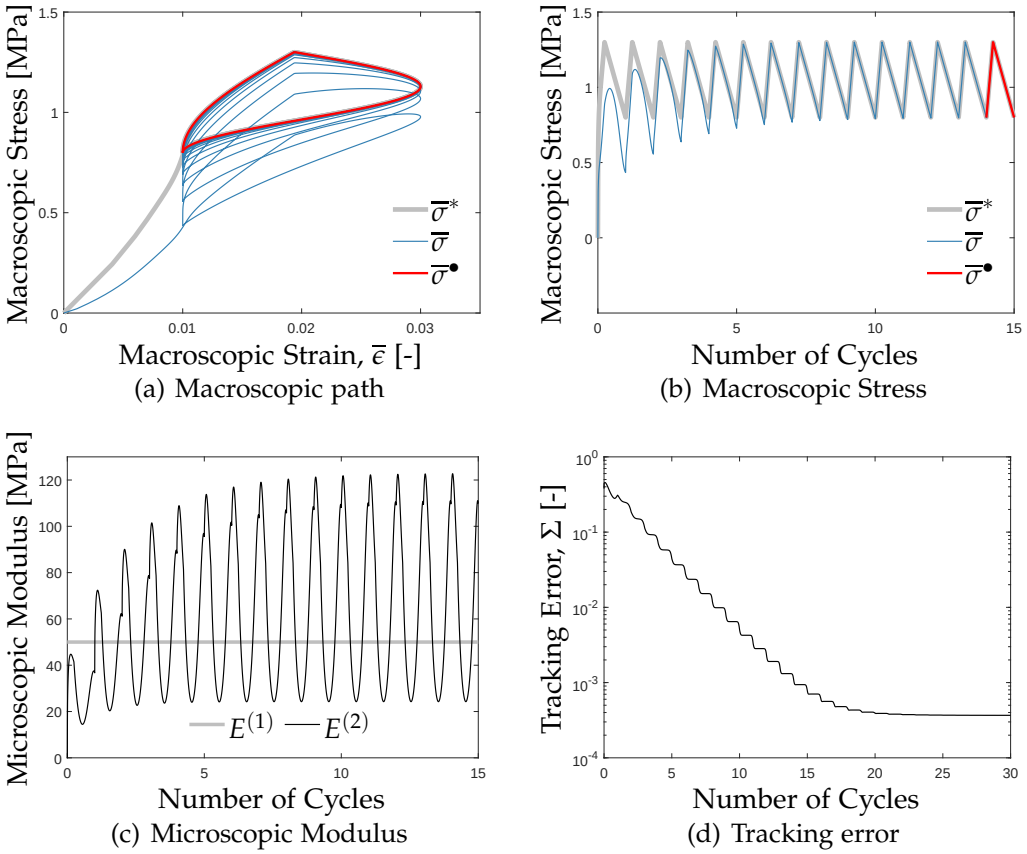

Figure 4.9: *Performance of the repetitive control system with proportional cascade controller*

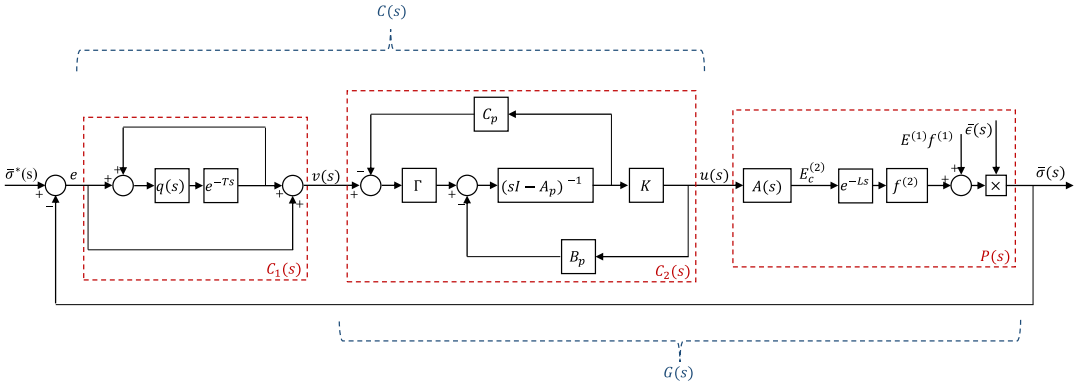

Figure 4.10: *Repetitive controller: full scheme*

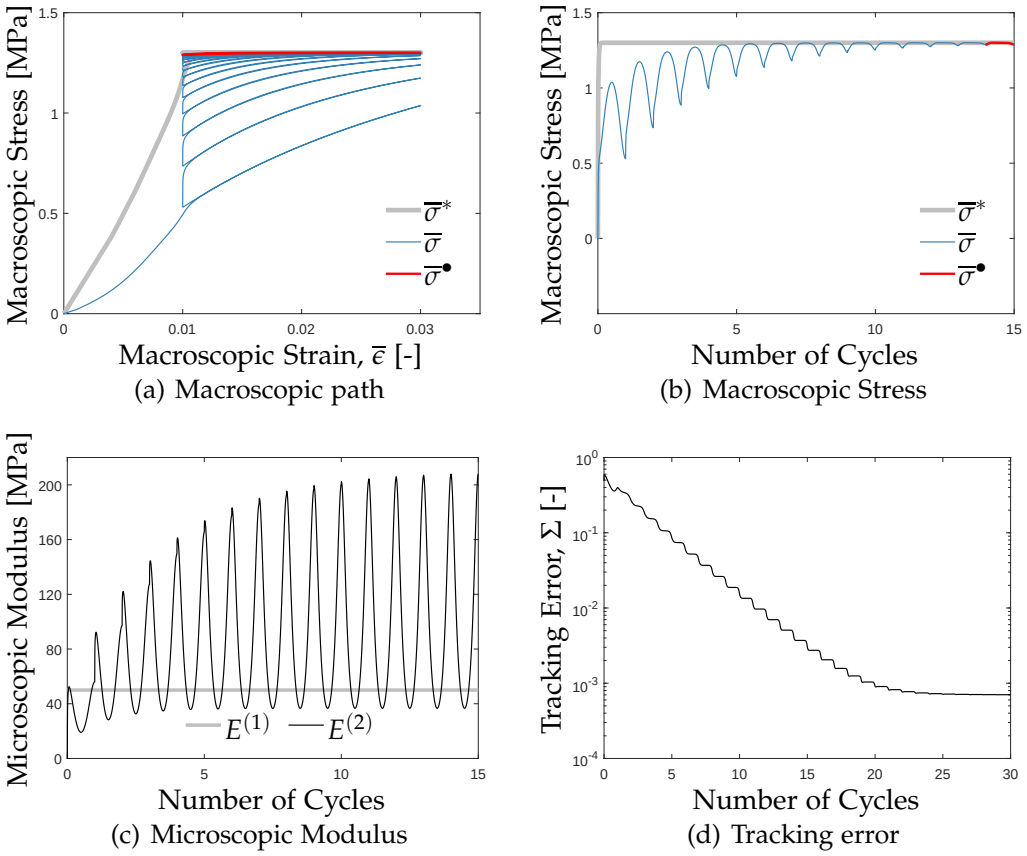

(a) Macroscopic path (b) Macroscopic Stress (c) Microscopic Modulus (d) Tracking error

Figure 4.11: *Performance of the repetitive control system with optimal state-space controller for the extreme case* $T_\sigma / T_\epsilon \to 0$.

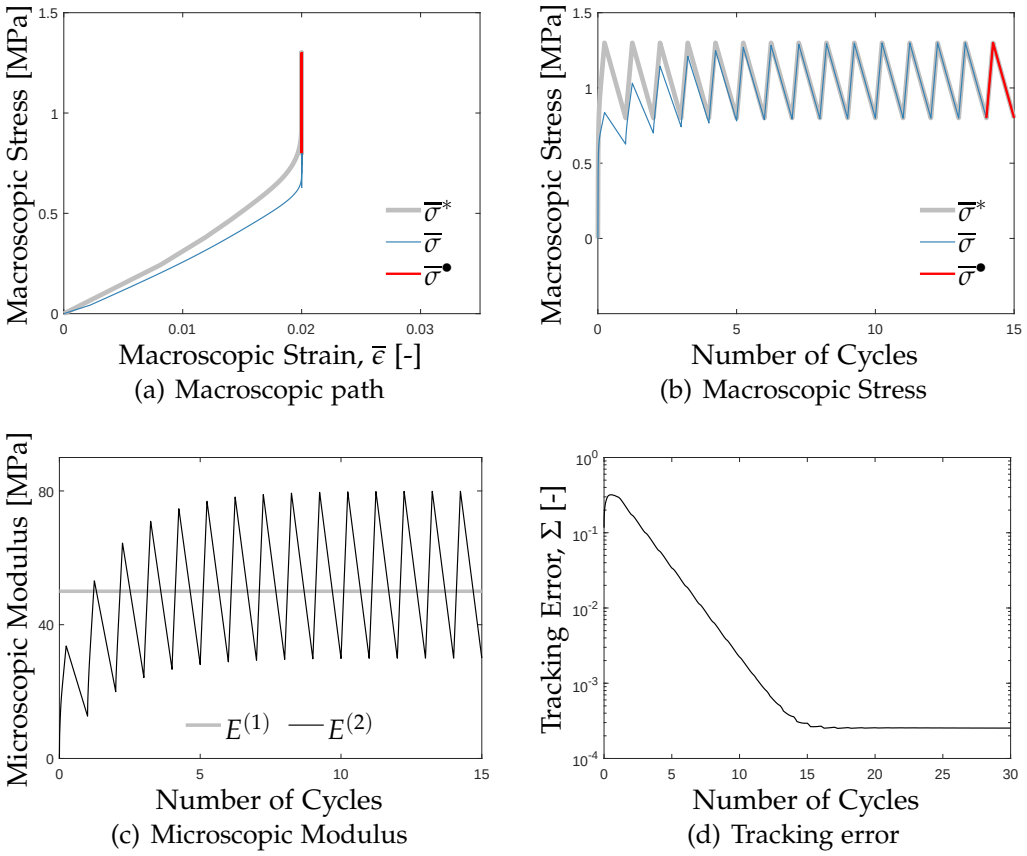

Figure 4.12: *Performance of the repetitive control system with optimal state-space controller for the extreme case* $T_\sigma / T_\epsilon \to \infty$.

Chapter 5

Control in Multi-Input Multi-Output (MIMO) Systems

5.1 Controller Design

In Chapter 4, design and analysis of control systems for SISO settings are discussed using three control approaches: PI controller, repetitive controller with proportional gain and repetitive controller with optimal state-space controller. In this chapter, control systems of MIMO settings (represented as in Figure 5.1) will be only discussed with the repetitive controller with optimal state-space controller. PI controller will not be used since design of PI controller for MIMO settings requires extra computation. For the each loop of the controlled system, stability analysis of the system and selection of the controller parameters are completed one by one. On the other hand, decoupling procedure is an another option while designing these controllers. The procedure can be applied to them as discussed in Section 3.1.1.2. Secondly, Repetitive controller with proportional gain will not be used since it also requires a proportional gain selection for each loop of the controlled system.

There are distinct benefits of using a MIMO approach for the design of the

controllers discussed here. Kalman filter gains of the optimal controller are nonetheless optimized while solving the Algebraic Riccati equation. By only selecting the values for Φ diagonal matrix, required gain values are determined for the coupled terms of the system (see Table 5.1).

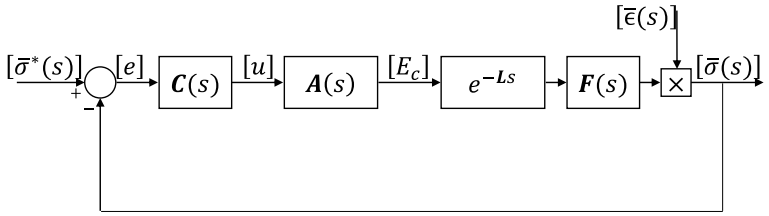

Figure 5.1: *Feedback control setup for MIMO settings*

5.1.1 Mathematical Modeling and Stability Analysis

Mathematical representation of the input-output relation in a MIMO system is constructed in matrix form. For example, the layered composite model under biaxial loading can be formulated as

$$\underbrace{\begin{bmatrix} \overline{\sigma}_{11}(t) \\ \overline{\sigma}_{22}(t) \end{bmatrix}}_{[\overline{\sigma}(t)]} = \underbrace{\begin{bmatrix} \overline{\epsilon}_{11}(t) & 0 \\ 0 & \overline{\epsilon}_{22}(t) \end{bmatrix}}_{[\overline{\epsilon}(t)]} \underbrace{\begin{bmatrix} \overline{E}_{\parallel}(t) \\ \overline{E}_{\perp}(t) \end{bmatrix}}_{[\overline{E}(t)]} \tag{5.1}$$

In Section 4.1.1, the nonlinear elastic modulus relation $\overline{E}_{\perp}(t)$ is linearized as 4.5 for stability analysis. This is also necessary for MIMO systems. Macroscopic stress $\overline{\sigma}_{22}(t)$ is therefore written in the linearized form so that the relation 5.1 becomes

$$\begin{bmatrix} \overline{\sigma}_{11}(t) \\ \overline{\sigma}_{22}(t) \end{bmatrix} = \epsilon(t) \begin{bmatrix} f^{(1)} & f^{(2)} \\ f^{(1)^*} & f^{(2)^*} \end{bmatrix} \begin{bmatrix} {E_c}^{(1)}(t) \\ {E_c}^{(2)}(t) \end{bmatrix} \tag{5.2}$$

where the strain relation is same along both axes: $\overline{\epsilon}_{11}(t) = \overline{\epsilon}_{22}(t) = \epsilon(t)$. The feedback controller scheme for this biaxial loading is depicted in Figure 5.2. The constants $f^{(1)^*} = 0.3359$ and $f^{(2)^*} = 0.6966$ are delivered from the linearization for ${E_c}^{(1)}(t_0) = 72.17$MPa and ${E_c}^{(2)}(t_0) = 58.30$MPa. Validation of the linearized elastic modulus with these constants versus the nonlinear modulus is showed in Figure 5.3 with a satisfactory comparison.

As mentioned previously, stability analysis of MIMO settings is performed with repetitive control methods where the cascade controller $C_2(s)$ is the optimal state-space controller. Repetitive control methods are suitable for both SISO and MIMO settings. The plant model for MIMO case in matrix form becomes

$$\mathbf{P}(s) = \widehat{\epsilon} e^{-Ls} \mathbf{F}(s) A(s) \tag{5.3}$$

The infinity norm stability analysis from 3.21 is

$$\left\| q(s)(I + \mathbf{G}(s))^{-1} \right\|_{\infty} < 1 \tag{5.4}$$

It is important to note that in this study, controller filter $p(s)$, actuator dynamics $A(s)$, and time delay e^{-Ls} are all in scalar form since they are selected similarly for each control loop. However, these system parameters can be defined differently, if needed.

5.1.2 Layered Composite under Biaxial Loading

As an example for the MIMO setting, layered composite under biaxial loading is performed. Control system parameters of this setting are presented in Table 5.1 where weight parameters for controller design are selected as $\Phi = diag(\sqrt{20000}, \sqrt{20000})$, $R = diag(1, 1)$ and $Q = diag(10^6, 10^6)$.

$\mathbf{P}(s)$	Γ	K	$\|\cdot\|_\infty$
$\begin{bmatrix} 0.5 & 0.5 \\ 0.6966 & 0.3359 \end{bmatrix} \frac{0.03}{1+0.0055s}$	$\begin{bmatrix} 92.15 & 326.11 \\ 233.95 & 92.15 \end{bmatrix}$	$\begin{bmatrix} 913.13 & 0 \\ 0 & 913.13 \end{bmatrix}$	0.912

Table 5.1: *System parameters for layered composite model where the low pass filter* $q(s) = \frac{1}{1+0.0008s}$.

In Figure 5.4, microstructure geometry and loading scenario are given for the layered composite model. The macroscopic stress relations are $\overline{\sigma}_{11}(t) = \overline{\epsilon}(t)\overline{E}_{\|}(t)$ and $\sigma_{22}(t) = \overline{\epsilon}(t)\overline{E}_{\perp}(t)$ from (2.3) (or also from (5.1)). each macroscopic response is controlled with microscopic moduli ${E_c}^{(1)}$ and ${E_c}^{(2)}$. Performance of this model is given in Figure 5.5. Tracking errors for both macroscopic responses decrease to desirable values in a satisfactory time period. Results show that target signals can be tracked in multi-loading cases with tunable constituents where the target signals are realizable, in other words microstructure is suitable for the adaptation space.

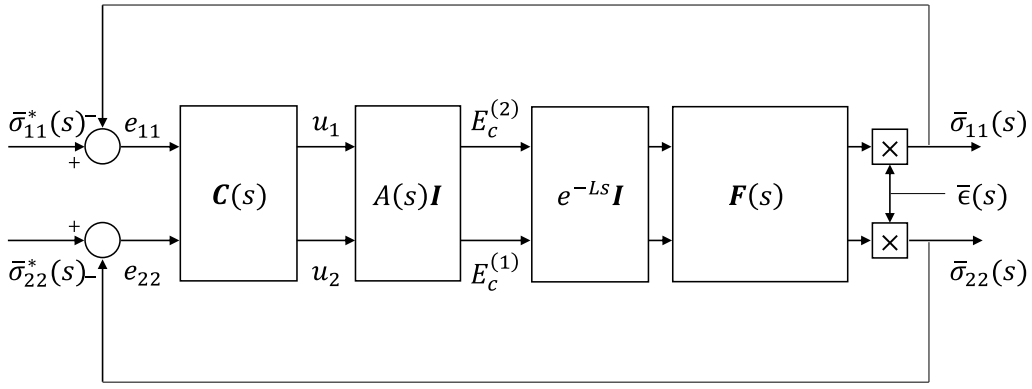

(a) Feedback control design for a two-input two-output System

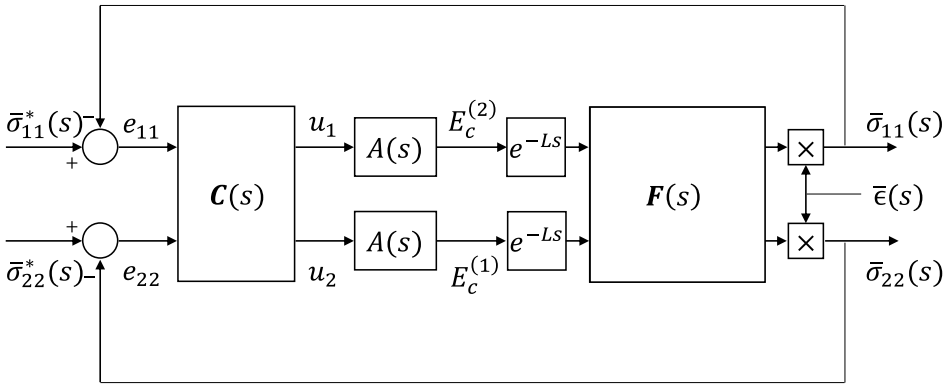

(b) Example case where $f^{(1)} = f^{(2)} = 0.5$, $f^{(1)^*} = 0.3359$ and $f^{(2)^*} = 0.6966$.

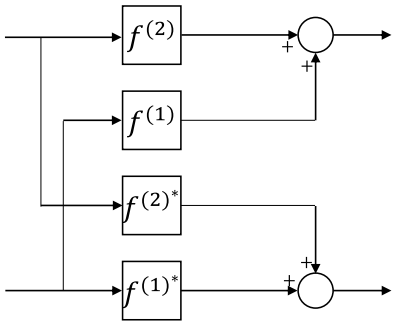

(c) Block diagram of $\mathbf{F}(s)$

Figure 5.2: *Feedback control system for layered composite model*

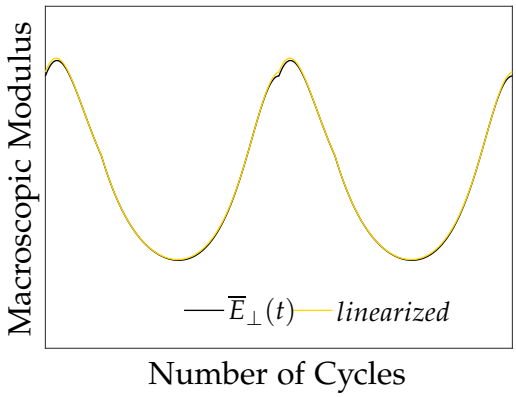

Figure 5.3: *Comparison of nonlinear and linearized microscopic elastic modulus for the MIMO case*

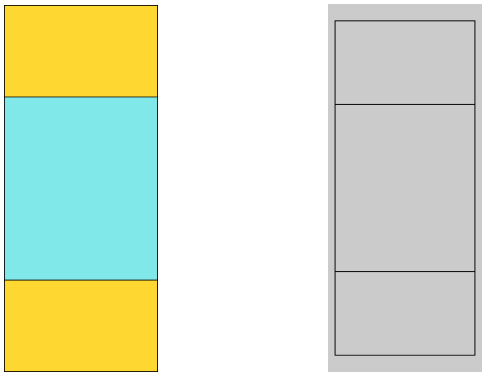

(a) Microstructure (b) Loading

Figure 5.4: *The microstructure geometry and the loading scenario are depicted for the layered composite of Section 5.1.2. Here, as well as in similar figures which follow, $E^{(2)}$ is associated with the turquoise constituent while the remaining constituent is assigned $E^{(1)}$ (with $f^{(1)} = f^{(2)} = 0.5$) and the horizontal (vertical) direction is denoted with 1 (2). Presently, loading is biaxial so that $\overline{\epsilon}_{11} \neq 0$ and $\overline{\epsilon}_{22} \neq 0$ while $\overline{\epsilon}_{12} = 0$. The deformed configuration is superposed over the initial one at an instant of loading in scaled form.*

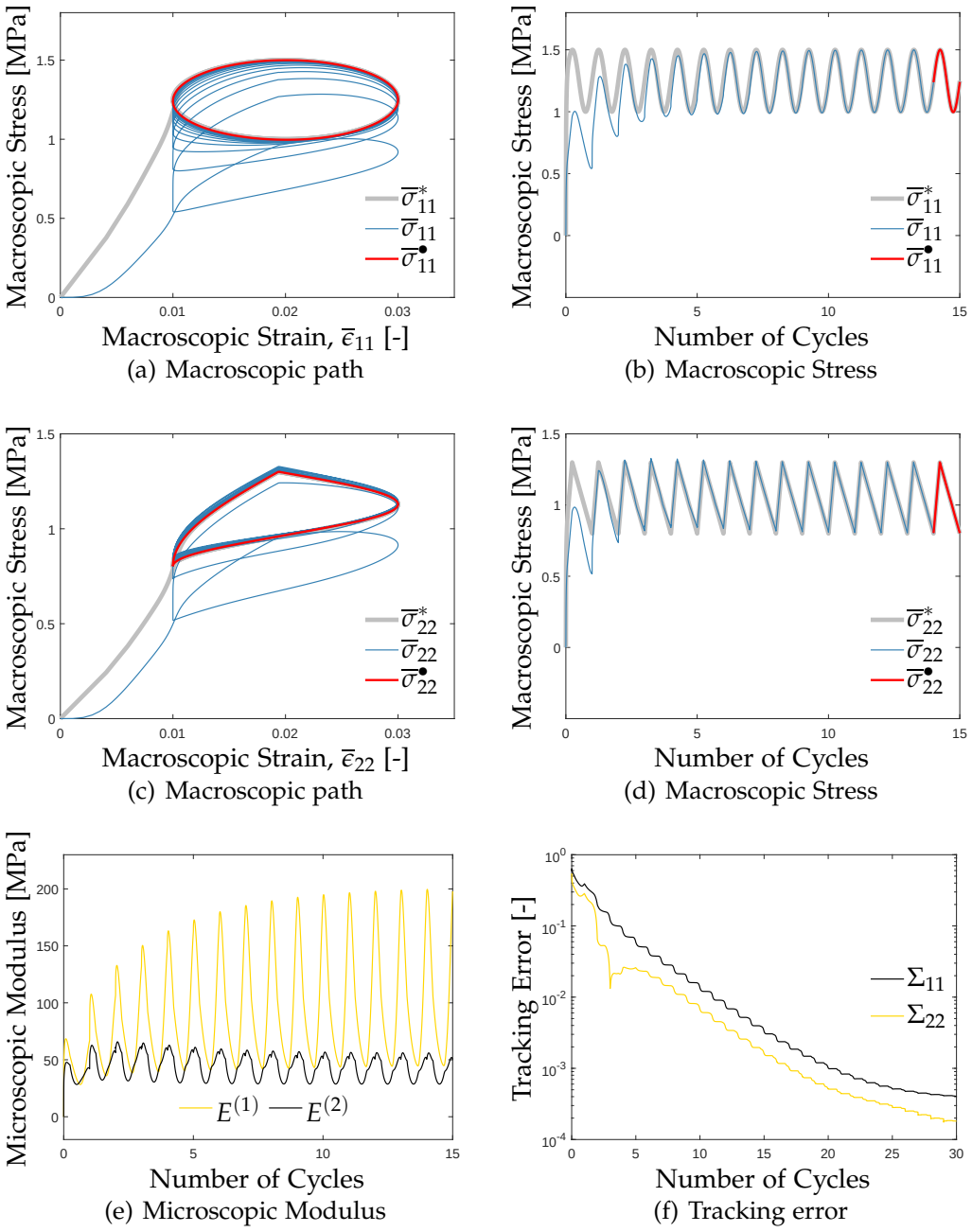

(a) Macroscopic path (b) Macroscopic Stress

(c) Macroscopic path (d) Macroscopic Stress

(e) Microscopic Modulus (f) Tracking error

Figure 5.5: *The controller performance is demonstrated for the layered composite of Section 5.1.2. Here, $\overline{\sigma}^*_{11}$ is constructed using cyc = cos with $T_\sigma = T_\epsilon$ and $\theta = \pi/2$ (see Figure 2.2) whereas $\overline{\sigma}^*_{22}$ is based on the default signal from Figure 2.3. All non-zero strain components (presently $\{\overline{\epsilon}_{11}, \overline{\epsilon}_{22}\}$) have the same variation* (2.5) *in all multi-dimensional examples.*

Chapter 6

FEM Based Simulations

6.1 Numerical Setup

Non-trivial microstructures will be employed in this chapter in order to show the versatility of the overall control framework. These microstructures are constructed in a FEM-based computation environment (i.e. COMSOL Multiphysics Structural Mechanics environment). The solution of a single boundary value problem therefore will be of concern at each time step so that computation time increases dramatically. However, development in a FEM-based computation environment without knowing their exact macroscopic mathematical model will help the feasibility and the generality of the control framework. As the main discussion is periodic microstructures in this study, periodic boundary conditions are adopted on the microstructure. For the material properties of each microstructure, constituents are assumed isotropic linearly elastic with zero Poisson's ratio in order to leave the elastic modulus as the only material parameter for simplicity.

In a general MIMO setting, the number n of input variables of the control system is equal to the number of output variables. For the single or multi-dimensional settings, d denotes the mechanical (M) dimension and it governs

overall cost of the simulation, and the variable number n denotes the control (C) governs the complexity of the control problem. The symbol MdCn therefore takes a place for the each microstructure model. Therefore, all the microstructure models are developed with a suitable adaptation space for the control problems. The FEM mesh resolution for the microstructures will be given in corresponding figures, and the time resolution is fixed in all systems where the period is traversed with 10000 steps. Moreover, with respect to (2.5), the macrostructure strain signal is set using $\{\overline{\epsilon}_o, \Delta\overline{\epsilon}, T_\epsilon\} = \{0.02, 0.01, 5\,\mathrm{s}\}$.

Note that the determination of an approximate mathematical model for the control system design is essential. On the other hand, these microstructures are designed directly in the FEM environment without a mathematical model. Different stress responses under a constant strain are thus examined for various elastic modulus parameters in order to find a mathematical representation. Later, for nonlinear relations, linearization is done with Taylor expansion as in Section 4.1.1.

6.2 Two-Dimensional Mechanics

6.2.1 One-Variable Control (M2C1)

The particular microstructure in Figure 6.1 demonstrates unit-cell of M2C1 microstructure. It is subjected to shear and target shear signal is selected as the default signal in Figure 2.3. As a second example for this model, a target signal with $T_\sigma/T_\epsilon = 0.5$. Figure 6.2 and Figure 6.3 give the performance results of the control systems for these two different target signals. The matrix of unit-cell is decided as fixed with $E^{(1)} = 150$MPa. It is important to observe that if $E^{(1)}$ is a large value, the target signal may not be feasible due to highly stiff shear response of the matrix model. On the other hand, for a small $E^{(1)}$ value, stiffness of the controlled pair wants to be very large and it may lead to also unfeasible signal demand and may increase the settling time of the

system as it takes more time to reach a higher value.

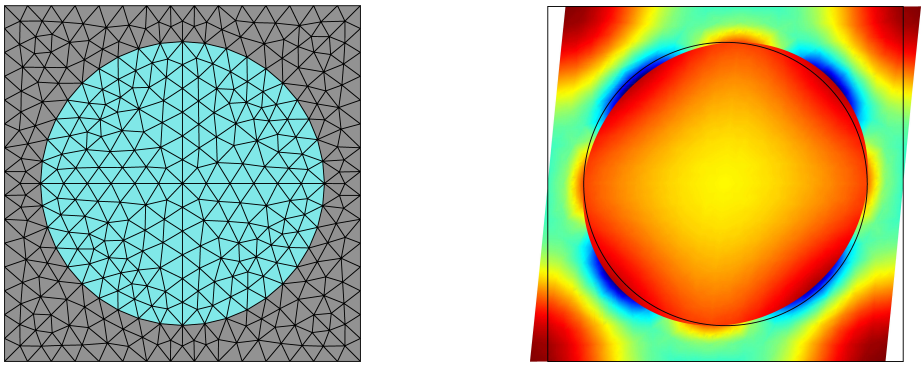

(a) Microstructure (b) Loading

Figure 6.1: *The microstructure geometry and the loading scenario ($\overline{\epsilon}_{12} \neq 0$) are depicted for the M2C1 setup. Here, $f^{(1)} = f^{(2)} = 0.5$ and only the particle elastic modulus $E^{(2)}$ is variable. The color distribution on the deformed configuration (scaled, at an instant of loading) is shown as an indicator for the magnitude of the shear stress, with red corresponding to maximum and blue corresponding to minimum value.*

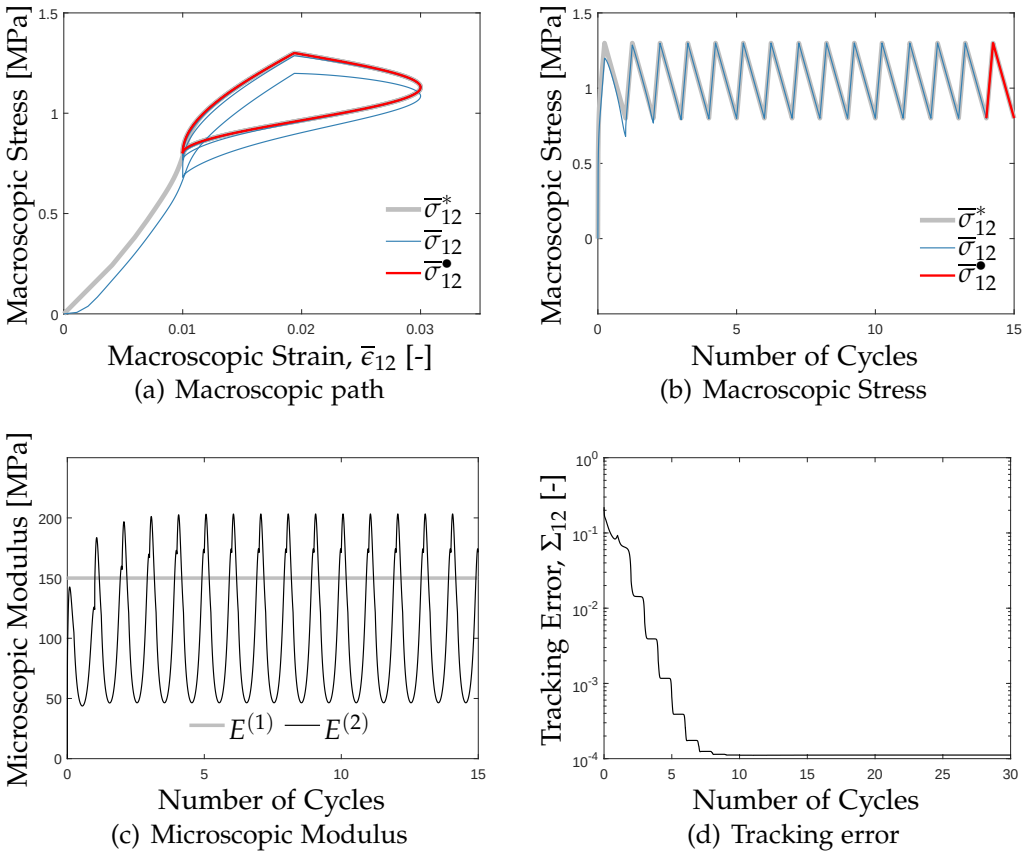

(a) Macroscopic path (b) Macroscopic Stress (c) Microscopic Modulus (d) Tracking error

Figure 6.2: *The controller performance is demonstrated for the first M2C1 setup.*

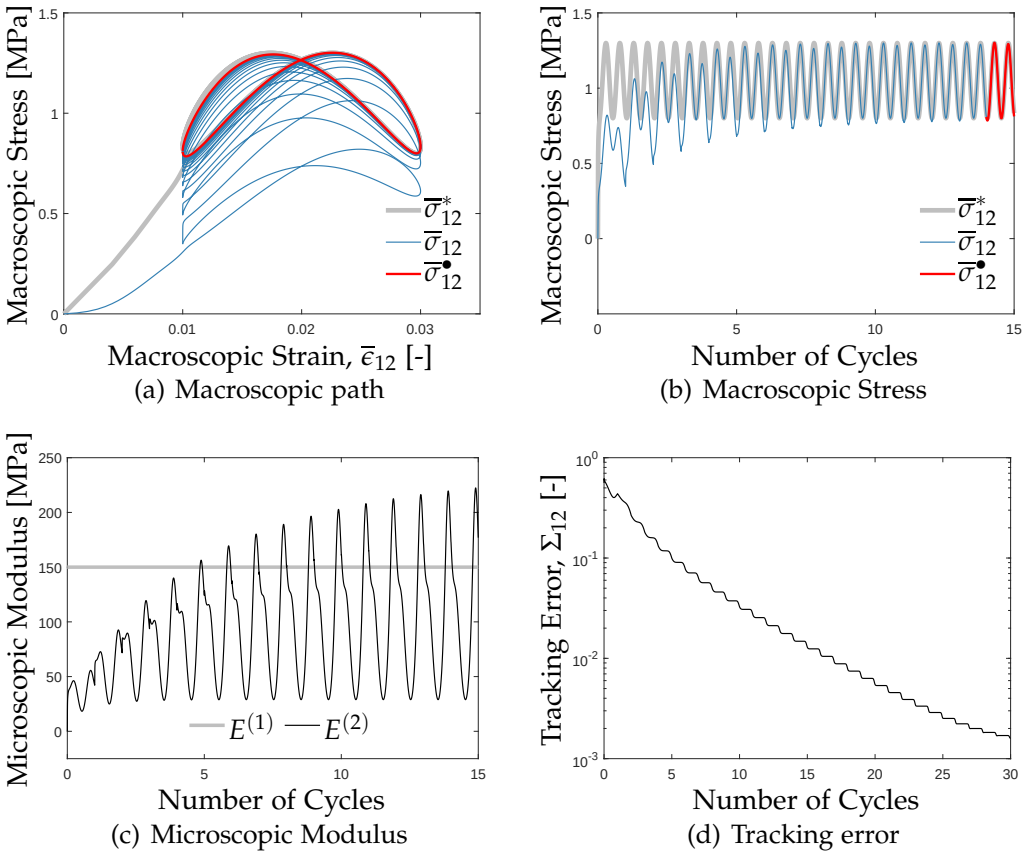

Figure 6.3: *The controller performance is demonstrated for the second M2C1 setup.*

6.2.2 Two-Variable Control (M2C2)

Model of M2C2 is given in Figure 6.4. This unit-cell is subjected to biaxial loading with same target signals with layered composite in Section 5.1.2 As the input signals and the loading are similar, the performances of these models are also close to each other. Consequently, it clearly shows that, it is possible to get identical responses from two tunable composites with entirely different microstructures. Figure 6.5 displays the performance of the control system.

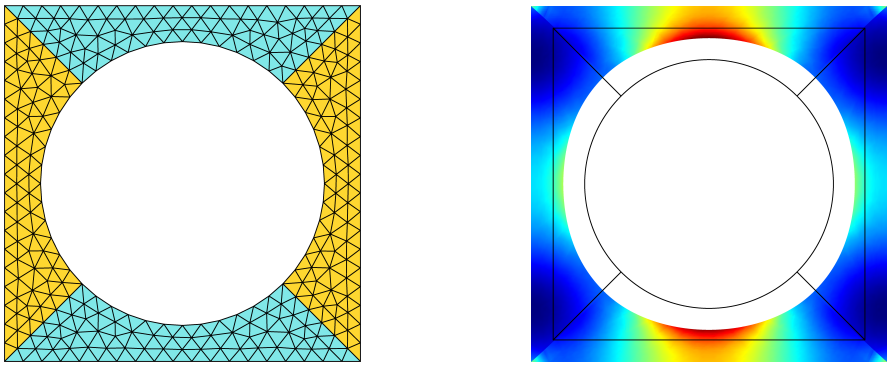

(a) Microstructure (b) Loading

Figure 6.4: *The microstructure geometry and the loading scenario ($\overline{\epsilon}_{11} \neq 0$ and $\overline{\epsilon}_{22} \neq 0$) are depicted for the M2C2 setup. Both constituents are tunable with a cell fraction $f^{(1)} = f^{(2)} = 0.25$, each contributing predominantly to the stress component along its individual axis of orientation. The color distribution on the deformed configuration (scaled, at an instant of loading) is shown as an indicator for the magnitude of the equivalent (von Mises) stress, with red corresponding to maximum and blue corresponding to minimum value.*

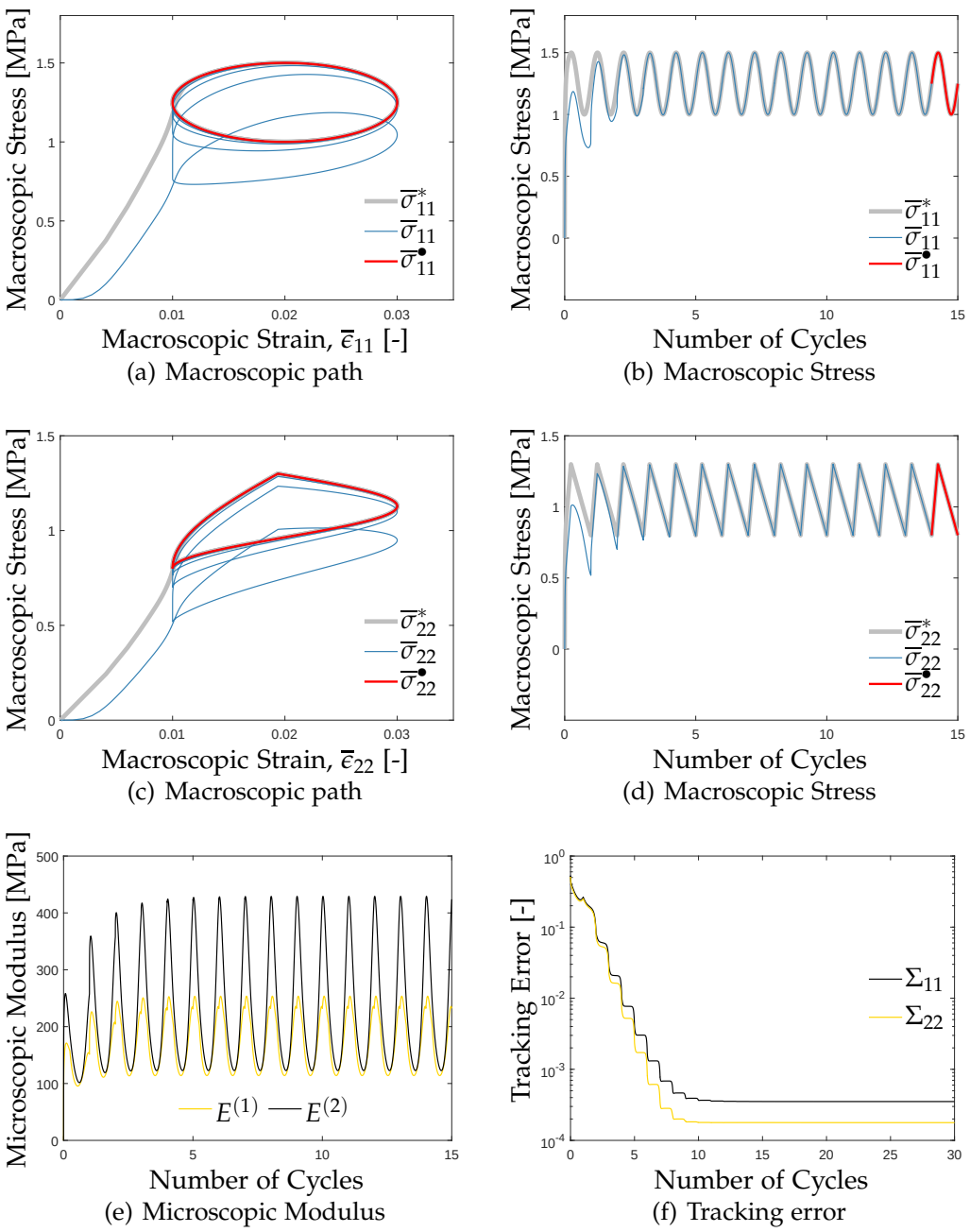

Figure 6.5: *The controller performance is demonstrated for the M2C2 setup of Section 6.2.2.*

6.2.3 Three-Dimensional Mechanics

In order to validate the feasibility of tunable mechanics, M3C1 unit-cell model is considered in Figure 6.6. The microstructure model is assigned with a porous nature, so $E^{(1)} = 0$. Under shear stress signals, two different target stress signals are targeted as in Figure 6.7 and Figure 6.8 where the first target signal is the default signal and the other employs $T_\sigma / T_\epsilon = 0.33$ respectively. The control problem targets a single shear stress signal by tuning a single elastic material $E^{(2)}$. Macroscopic response of the microstructure however is anisotropic even though its microscopic constituents are isotropic, so that tuning can help control this anistropic behavior in a structural application on the macroscale.

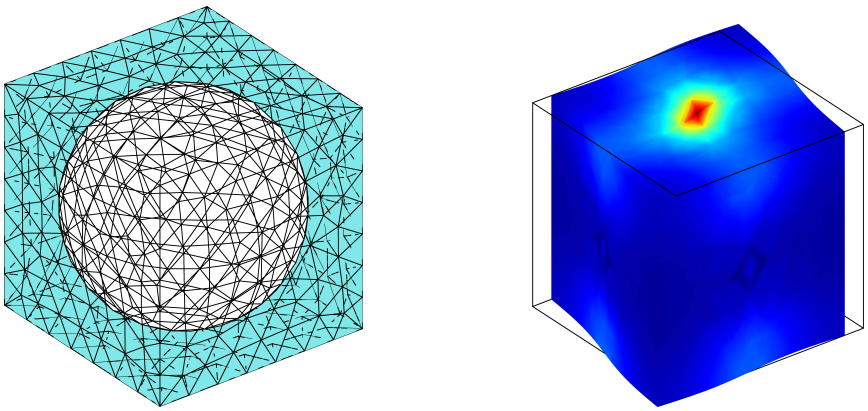

(a) Microstructure (b) Loading

Figure 6.6: *The microstructure geometry and the loading scenario ($\overline{\epsilon}_{13} \neq 0$) are depicted for the M3C1 setup. The pore ($E^{(1)} = 0$) leaves the particle elastic modulus $E^{(2)}$ as the only variable with $f^{(1)} = f^{(2)} = 0.5$. The color distribution on the deformed configuration (scaled, at an instant of loading) is shown as an indicator for the magnitude of the shear stress, with red corresponding to maximum and blue corresponding to minimum value.*

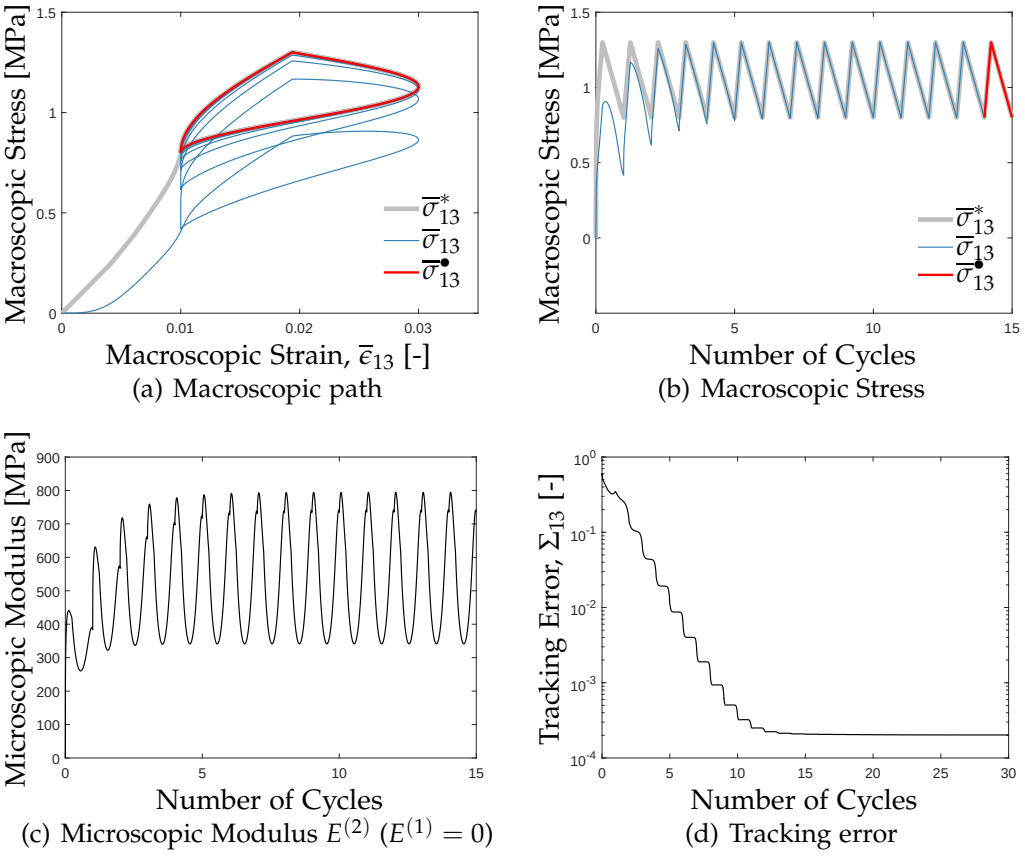

(a) Macroscopic path (b) Macroscopic Stress

(c) Microscopic Modulus $E^{(2)}$ ($E^{(1)} = 0$) (d) Tracking error

Figure 6.7: *The controller performance is demonstrated for the first M3C1 setup*

Model	Mathematical Model	Parameters
M2C1	$\overline{E}_{12} = (f^{(1)}{E^{(1)}}^n + f^{(2)}{E_c^{(2)}}^n)^{1/n}$	$f^{(1)} = f^{(2)} = 0.5$, $n = -0.87$
M2C2	$\overline{E}_{11} = (f^{(1)}{E^{(1)}}^n + f^{(2)}{E_c^{(2)}}^n)^{1/n}$ $\overline{E}_{22} = (f^{(2)}{E^{(1)}}^n + f^{(1)}{E_c^{(2)}}^n)^{1/n}$	$f^{(1)} = 1.255$, $f^{(2)} = 0.1654$ $n = -0.2919$
M3C1	$\overline{E}_{13} = f^{(2)}{E_c^{(2)}}^n$	$f^{(2)} = 0.1071$, $n = 1.002$

Table 6.1: *System parameters for FEM-based simulations*

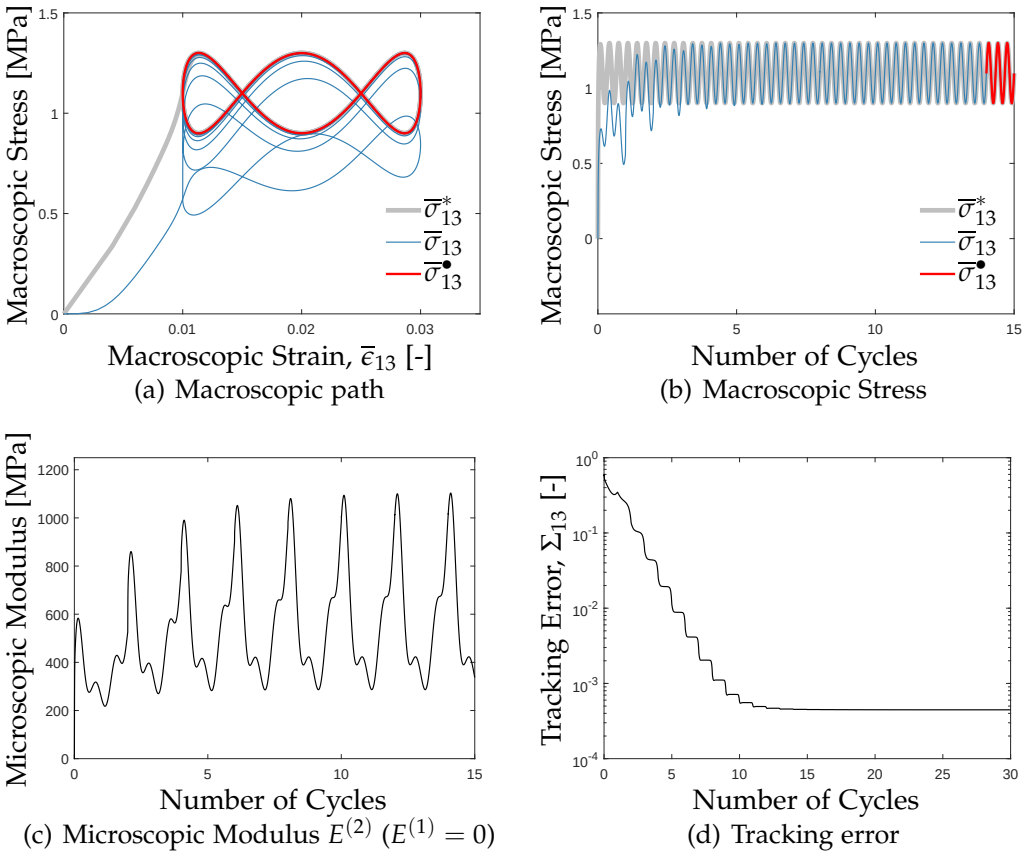

(a) Macroscopic path (b) Macroscopic Stress

(c) Microscopic Modulus $E^{(2)}$ ($E^{(1)} = 0$) (d) Tracking error

Figure 6.8: *The controller performance is demonstrated for the second M3C1 setup.*

Chapter 7

Discussion

The goal of the study was to examine smart composites which perform optimally under time-varying performance criteria. This goal was accomplished with numerical settings in three major steps: (1) the presentation of capabilities provided by specified composites, which establishes the requirements on the numerical approach, (2) development of control systems which are suitable for mechanics in multiple dimensions, and (3) the integration of a general computational method within a control system in order to address realistic microstructures. For the practical applications, tuning of the smart composites was realized for periodic signals through repetitive controllers. Various examples, which have complex paths in stress-strain space that cannot be achieved by any combination of traditional materials, were demonstrated to show the success of these controllers. In conclusion, FEM-based simulations are performed to examine the feasibility of the study in both two and three-dimensional settings. For the numerical studies, MATLAB and Simulink softwares are used, and control systems were simulated via Simulink. For the FEM-based analyses, COMSOL Multiphysics was used as the FEM environment by embedding COMSOL server to Simulink.

Various challenges remain to be addressed from a control perspective, such as the uncertainties in material behavior as well as the time delays from the

actuators and the sensors. For example, if the uncertainty limits of an uncertain parameter of the plant dynamics cannot be defined properly and this parameter exceeds the assigned values, the system may be unstable. Moreover, if the selected actuator or sensor has a low response time, it has large time delay on it. It may lead to performance decrease in tracking or instability. However, a number of issues specifically stand out as particular topics for future research. For instance, composite manufacturing with desired materials might be difficult to achieve, or it might be impossible to model dynamic properties of the smart materials. Note that mathematical modeling of the system dynamics is necessary for control system design and analysis. An approximated model can be achieved through the frequency response analysis of the material via an experimental setup or a finite element method environment. From frequency analysis, an approximated transfer function can be therefore obtained. Finally, experimental studies involving the control of a smart material system may indicate needs for further improvements to the numerical modeling or the control setup itself towards a more comprehensive and reliable tuning framework.

Bibliography

[1] S. Hara, Y. Yamamoto, T. Omata, and M. Nakano, "Repetitive control system: a new type servo system for periodic exogenous signals," *IEEE Transactions on Automatic Control*, vol. 33, pp. 659–668, July 1988.

[2] A. K. Kaw, *Mechanics of Composite Materials*. Boca Raton: CRC Press, 2nd ed., 2005.

[3] T. I. Zohdi, "Constrained inverse formulations in random material design," *Computer Methods in Applied Mechanics and Engineering*, vol. 192, pp. 3179–3194, 2003.

[4] J. K. Guest, "Optimizing the layout of discrete objects in structures and materials: A projection-based topology optimization approach," *Computer Methods in Applied Mechanics and Engineering*, vol. 283, pp. 330 – 351, 2015.

[5] C. Kiyono, E. Silva, and J. Reddy, "Design of laminated piezocomposite shell transducers with arbitrary fiber orientation using topology optimization approach," *International Journal for Numerical Methods in Engineering*, vol. 90, no. 12, pp. 1452–1484, 2012.

[6] A. Khani, M. M. Abdalla, and Z. Gürdal, "Optimum tailoring of fibre-steered longitudinally stiffened cylinders," *Composite Structures*, vol. 122, pp. 343–351, 2015.

[7] J.-H. Lee, J. P. Singer, and E. L. Thomas, "Micro-/nanostructured mechanical metamaterials," *Adv. Mater.*, vol. 24, pp. 4782–4810, 2012.

[8] M. P. Bendsøe and O. Sigmund, *Topology Optimization: Theory, Methods and Applications*. Springer, 2nd ed., 2004.

[9] P. W. Christensen and A. Klarbring, *An Introduction to Structural Optimization*. Springer, 2010.

[10] O. Sigmund and S. Torquato, "Composites with extremal thermal expansion coefficients," *Appl. Phys. Lett.*, vol. 69, pp. 3203–3205, 1996.

[11] O. Sigmund, "A new class of extremal composites," *Journal of the Mechanics and Physics of Solids*, vol. 48, pp. 397–428, 2000.

[12] B.-C. Chen, E. C. N. Silva, and N. Kikuchi, "Advances in computational design and optimization with application to MEMS," *International Journal for Numerical Methods in Engineering*, vol. 52, no. 1-2, pp. 23–62, 2001.

[13] P. Nakshatrala, D. Tortorelli, and K. Nakshatrala, "Nonlinear structural design using multiscale topology optimization. part i: Static formulation," *Computer Methods in Applied Mechanics and Engineering*, vol. 261 - 262, pp. 167 – 176, 2013.

[14] J. Kato, D. Yachi, K. Terada, and T. Kyoya, "Topology optimization of micro-structure for composites applying a decoupling multi-scale analysis," *Struct Multidisc Optim*, vol. 49, pp. 595–608, 2014.

[15] A. Rafsanjani, A. Akbarzadeh, and D. Pasini, "Snapping mechanical metamaterials under tension," *Advanced Materials*, vol. 27, pp. 5931–5935, 2015.

[16] B. Haghpanah, L. Salah-Sharif, P. Pourrajab, J. Hopkins, and L. Valdevit, "Multistable shape-reconfigurable architected materials," *Advanced Materials*, vol. 28, pp. 7915–7920, 2016.

[17] D. Restrepo, N. D. Mankame, and P. D. Zavattieri, "Programmable materials based on periodic cellular solids. Part I: Experiments," *International Journal of Solids and Structures*, vol. 100-101, pp. 485–504, 2016.

[18] W. Shan, T. Lu, and C. Majidi, "Soft-matter composites with electrically tunable elastic rigidity," *Smart Mater. Struct.*, vol. 22, p. 085005, 2013.

[19] W. Shan, S. Diller, A. Tutcuoglu, and C. Majidi, "Rigidity-tuning conductive elastomer," *Smart Mater. Struct.*, vol. 24, p. 065001, 2015.

[20] M. Kallio, *The elastic and damping properties of magnetorheological elastomers*. PhD thesis, Tampere University of Technology, Tampere, Finland, 2005.

[21] W. H. Li, Y. Zhou, and T. F. Tian, "Viscoelastic properties of MR elastomers under harmonic loading," *Rheol Acta*, vol. 49, pp. 733–740, 2010.

[22] M. Kallio, T. Lindroos, S. Aalto, E. Järvinen, T. Kärnä, and T. Meinander, "Dynamic compression testing of a tunable spring element consisting of a magnetorheological elastomer," *Smart Mater. Struct.*, vol. 16, pp. 506–514, 2007.

[23] Y. Li, J. Li, W. Li, and H. Du, "A state-of-the-art review on magnetorheological elastomer devices," *Smart Mater. Struct.*, vol. 23, p. 123001, 2014.

[24] D. Lee, M. Lee, N. Jung, M. Yun, J. Lee, T. Thundat, and S. Jeon, "Modulus-tunable magnetorheological elastomer microcantilevers," *Smart Mater. Struct.*, vol. 23, p. 055017, 2014.

[25] N. D. Wanasekara, D. A. Stone, G. E. Wnek, and L. T. J. Korley, "Stimuli-responsive and mechanically-switchable electrospun composites," *Macromolecules*, vol. 45, no. 22, pp. 9092–9099, 2012.

[26] K. Nakanishi, F. Sassa, and K. Hayashi, "Photo-tunable molecular recognizing smart material for gas sensing," in *2017 19th International Conference on Solid-State Sensors, Actuators and Microsystems (TRANSDUCERS)*, pp. 1376–1379, June 2017.

[27] C.-Y. Lee, C.-C. Chen, T.-H. Yang, and C.-J. Lin, "Structural vibration control using a tunable hybrid shape memory material vibration absorber," *Journal of Intelligent Material Systems and Structures*, vol. 23, no. 15, pp. 1725–1734, 2012.

[28] K. D. Yao, T. Peng, M. F. A. Goosen, J. M. Min, and Y. Y. He, "ph-sensitivity of hydrogels based on complex forming chitosan: Polyether

interpenetrating polymer network," *Journal of Applied Polymer Science*, vol. 48, no. 2, pp. 343–354.

[29] D.-G. Hwang and M. D. Bartlett, "Tunable mechanical metamaterials through hybrid kirigami structures," *Scientific Reports*, vol. 8, no. 2, 2018.

[30] H. Zhang, X. Guo, J. Wu, D. Fang, and Y. Zhang, "Soft mechanical metamaterials with unusual swelling behavior and tunable stress-strain curves," *Science Advances*, vol. 4, no. 6, 2018.

[31] D. W. Wright and R. S. C. Cobbold, "The characteristics and applications of metamaterials," *Ultrasound*, vol. 17, no. 2, pp. 68–73, 2009.

[32] L. D'Alessandro, V. Zega, R. Ardito, and A. Corigliano, "3d auxetic single material periodic structure with ultra-wide tunable bandgap," *Scientific Reports*, vol. 8, no. 1, 2018.

[33] X. Zhao, J. Kim, C. A. Cezar, N. Huebsch, K. Lee, K. Bouhadir, and D. J. Mooney, "Active scaffolds for on-demand drug and cell delivery," *Proceedings of the National Academy of Sciences*, vol. 108, no. 1, pp. 67–72, 2011.

[34] D. Ge, E. Lee, L. Yang, Y. Cho, M. Li, D. S. Gianola, and S. Yang, "A robust smart window: Reversibly switching from high transparency to angle-independent structural color display," *Advanced Materials*, vol. 27, no. 15, pp. 2489–2495.

[35] N. W. Bartlett, M. T. Tolley, J. T. B. Overvelde, J. C. Weaver, B. Mosadegh, K. Bertoldi, G. M. Whitesides, and R. J. Wood, "A 3d-printed, functionally graded soft robot powered by combustion," *Science*, vol. 349, no. 6244, pp. 161–165, 2015.

[36] S. Shian, K. Bertoldi, and D. R. Clarke, "Dielectric elastomer based "grippers" for soft robotics," *Advanced Materials*, vol. 27, no. 43, pp. 6814–6819.

[37] Z.-F. Liu, B. Wu, and C.-F. He, "The properties of optimal two-dimensional phononic crystals with different material contrasts," *Smart Materials and Structures*, vol. 25, no. 9, p. 095036, 2016.

[38] X. Liu, T.-C. Tang, E. Tham, H. Yuk, S. Lin, T. K. Lu, and X. Zhao, "Stretchable living materials and devices with hydrogel–elastomer hybrids hosting programmed cells," *Proceedings of the National Academy of Sciences*, vol. 114, no. 9, pp. 2200–2205, 2017.

[39] M. C. Chiappelli and R. C. Hayward, "Photonic multilayer sensors from photo-crosslinkable polymer films," *Advanced Materials*, vol. 24, no. 45, pp. 6100–6104.

[40] C. Chen, *Linear System Theory and Design*. Oxford series in electrical and computer engineering, Oxford University Press, 2013.

[41] J. Doyle, B. Francis, and A. Tannenbaum, *Feedback control theory*. Macmillan Pub. Co., 1992.

[42] C. E. García, D. M. Prett, and M. Morari, "Model predictive control: Theory and practice—a survey," *Automatica*, vol. 25, no. 3, pp. 335 – 348, 1989.

[43] Y. Wang, L. Xie, and C. E. de Souza, "Robust control of a class of uncertain nonlinear systems," *Systems I& Control Letters*, vol. 19, no. 2, pp. 139 – 149, 1992.

[44] K. Zhou and J. Doyle, *Essentials of Robust Control*. Prentice Hall Modular Series for Eng, Prentice Hall, 1998.

[45] K. Zhou, J. Doyle, and K. Glover, *Robust and Optimal Control*. Feher/Prentice Hall Digital and, Prentice Hall, 1996.

[46] C. Desoer and M. Vidyasagar, *Feedback Systems: Input-output Properties*. Classics in Applied Mathematics, Society for Industrial and Applied Mathematics (SIAM, 3600 Market Street, Floor 6, Philadelphia, PA 19104), 1975.

[47] D. Seborg, D. Mellichamp, T. Edgar, and F. Doyle, *Process Dynamics and Control*. John Wiley & Sons, 2010.

[48] S. Nemat-Nasser and M. Hori, *Micromechanics: Overall Properties of Heterogeneous Materials*. North-Holland Series in Applied Mathematics and Mechanics, Elsevier Science, 1999.

[49] G. A. Pavliotis and A. M. Stuart, *Multiscale Methods: Averaging and Homogenization*. Springer-Verlag, 2008.

[50] S. Torquato, *Random Heterogeneous Materials: Microstructure and Macroscopic Properties*. Springer, Berlin Heidelberg New York, 2002.

[51] T. I. Zohdi and P. Wriggers, *Introduction to Computational Micromechanics*. Springer, Berlin Heidelberg New York, 2005.